NASA TECHNICAL NOTE

NASA TN D-3362

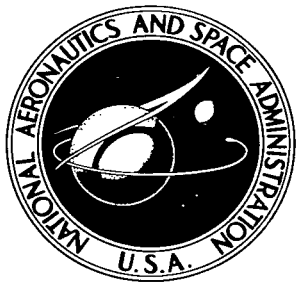

NASA TN D-3362

APOLLO INFRARED ACQUISITION AND TRACKING SYSTEM

by H. L. Richard

Goddard Space Flight Center
Greenbelt, Md.

NATIONAL AERONAUTICS AND SPACE ADMINISTRATION • WASHINGTON, D. C. • OCTOBER 1966

NASA TN D-3362

APOLLO INFRARED ACQUISITION AND TRACKING SYSTEM

By H. L. Richard

Goddard Space Flight Center
Greenbelt, Md.

NATIONAL AERONAUTICS AND SPACE ADMINISTRATION

For sale by the Clearinghouse for Federal Scientific and Technical Information
Springfield, Virginia 22151 – Price $2.50

ABSTRACT

When a spacecraft reenters the earth's atmosphere, the temperatures of its surface and the surrounding air reach high values as the air is decelerated and compressed. Since air at very high temperatures becomes electrically conductive, radio communication may be blacked out, as happened during the reentry of the Mercury and Gemini spacecraft. A much more serious communication and tracking blackout condition is expected for the Apollo vehicle's reentry at hypervelocity speeds, with the possibility of a blackout for 85 percent of the nominal 2,000 nautical mile reentry trajectory.

The same reentry heating phenomenon, however, will generate sufficient energy in the infrared band to permit acquisition and tracking at a range of 500 nautical miles from an aircraft flying at 35,000 feet. Although reentry-generated radiation ranges from ultraviolet to infrared, infrared radiation in the 3-5 micron range is considered the most suitable for acquiring and tracking the Apollo vehicle during reentry. Ultraviolet radiation from the shock layer is seriously attenuated by the atmosphere and the ultraviolet as well as the visible and near-infrared radiation from ablation effects would be difficult to detect in the sunlit sky background of the planned daylight reentry. Also, during any trajectory skip period where there is less ultraviolet or visible radiation, infrared acquisition and tracking of the heated spacecraft would still be possible. Furthermore, atmospheric effects such as scattered sunlight and atmospheric thermal emission present a background radiation with a minimum radiance across a 3-5 micron infrared band. This also conveniently falls at a "window" in the atmosphere where infrared transmission is especially high, namely the 3-5 micron band.

Cloud coverage between the target and the sensor would seriously attenuate the signal received by any infrared tracking device. However, in view of the findings of the U. S. Weather Bureau that cloud cover over the reentry area above 35,000 feet should be minimal and the fact that eight service aircraft would be deployed to cover the reentry, cloud coverage is not considered a serious problem.

Clouds not in the line of sight but within search range could appear as a target on the operator's screen. Other sources of background radiation which must be considered as possible false targets include stars, platform and optics radiation, aircraft appendages and the Apollo Service Module, which could be reentering the earth's atmosphere at about the same time and in near proximity to the real target. Discrimination against false targets may be exercised by utilization of an operator and by discrimination circuitry.

A study undertaken to define boundary values for the maximum and minimum infrared radiation the Apollo spacecraft could generate indicates that the surface temperatures of the spacecraft, based on calculations of convective and radiative heat input rates, will be between a 1000°K ablation and a 2500°K equilibrium temperature. With the minimum target temperature, a conservative atmospheric transmissivity of 70 percent, and 37 percent of the source radiant energy falling within the wavelength response of the infrared system, calculation of the total amount of radiation at the optical aperature of the system gives a value of 4.9×10^{-12} watts/cm^2 at a range of 500 nautical miles.

The calculated irradiation at the aperature and the sensitivity of a detector system utilizing components now available would give a signal-to-noise ratio of about 6.5. More recent work by the University of Michigan utilizing Apollo heat rate input data verifies the detection range capability and the choice of detection waveband. Existing optical systems and components permit the development of an infrared hemispherical scanner capable of meeting the design requirements of search, track and lock-on at the desired wavelengths and sensitivity levels.

CONTENTS

APOLLO INFRARED ACQUISITION AND TRACKING SYSTEM

by
H. L. Richard
Goddard Space Flight Center

INTRODUCTION

When a spacecraft reenters the earth's atmosphere, it dissipates a considerable amount of kinetic energy. Most of this energy is transformed into heat as the air about the spacecraft is decelerated and compressed. Dissociation and thermal ionization of the air occurs and as a result radiant energy is released.

Temperatures on the surface of the spacecraft reach high values predominately as a result of the convective heat transfer. An additional heat input is the radiative heat transfer from the air radiation.

It is not only the aerodynamic heating problem which is of interest, but the fact that at very high air temperatures the air about the spacecraft becomes electrically conductive, introducing new problems in radio wave transmission and reception. In the most critical case, radio communication is completely blacked out. This blackout condition has already been experienced during the reentry of the Mercury and Gemini spacecraft. A much more serious condition of tracking and communication blackout is expected for spacecraft reentering the earth's atmosphere at hypervelocity speeds, which is the case for the Apollo vehicle on return from a lunar mission. It is particularly critical since its occurrence will coincide with the maneuver phase of the spacecraft (Figure 1). This loss in communications may severely limit the ground support during a vital portion of this phase or even during the entire regime of reentry flight, depending upon the type of reentry trajectory. Figure 2 depicts a nominal trajectory of 2,000 nautical mile range. Indicated are the expected communication blackout boundaries. In this case, blackout could occur for 85 percent of the reentry distance travelled.

Directing our attention to this problem, we have investigated the capability of an infrared search and track system which would acquire the Apollo spacecraft from the self-generated, thermal heating—the same phenomenon which caused the communication blackout.

The convective and radiative heating effects to the spacecraft during reentry will cause the exterior to reach such temperatures that the spacecraft is essentially and literally a "blackbody" radiating energy predominately in the infrared part of the spectrum.

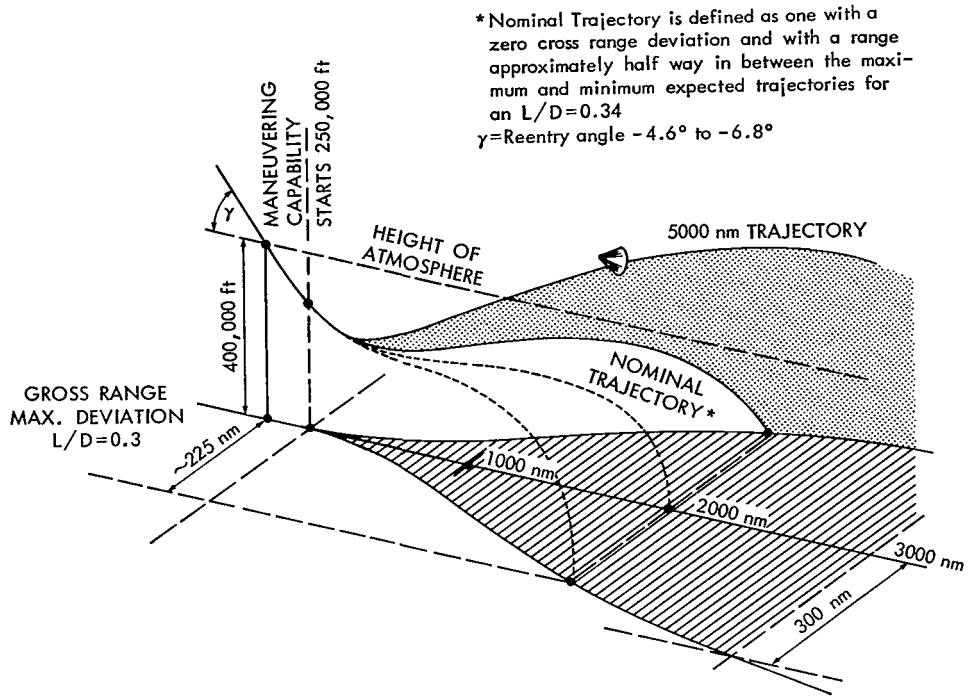

Figure 1—Down range and cross range footprint for maneuvering Apollo spacecraft (from Reference 1).

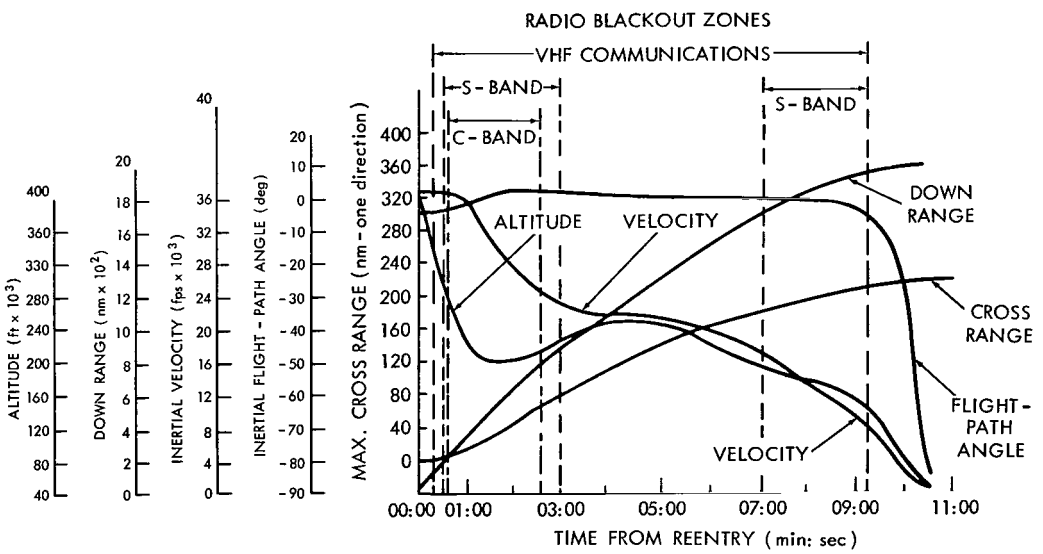

Figure 2—Typical trajectory parameters as a function of time for an initial flight-path angle of -6.4° and a reentry range of 2000 nm, L/D = 0.4. Indicated are the radio blackout zones (References 1 and 2).

It is this radiant energy which would be utilized by a passive infrared system, a system requiring no weight, power, or space on board the Apollo spacecraft. It also requires no large ship or real estate and is highly mobile, so that for any unforeseen event it can quickly span continents and oceans to be on site during a spacecraft reentry.

Fundamentally, the infrared acquisition and tracking system (IRATS) could serve to

1. point and slave the unified S-band communication antenna on board the Apollo range instrumented aircraft,
2. provide angle track data for trajectory calculations in real time, and
3. provide data for postflight analysis.

A more complete description of the IRATS requirements and operation is given in the GSFC Specification, "Infrared Acquisition and Tracking System." This specification was written for the development of a system to perform the above functions from aircraft cruising at approximately 35,000 feet.

In examining the infrared radiance characteristics of the reentering Apollo spacecraft, it is well to examine the total spectral radiance characteristics (source signal characteristics) of a body reentering the earth's atmosphere at super-orbital velocities. On this basis, one can then

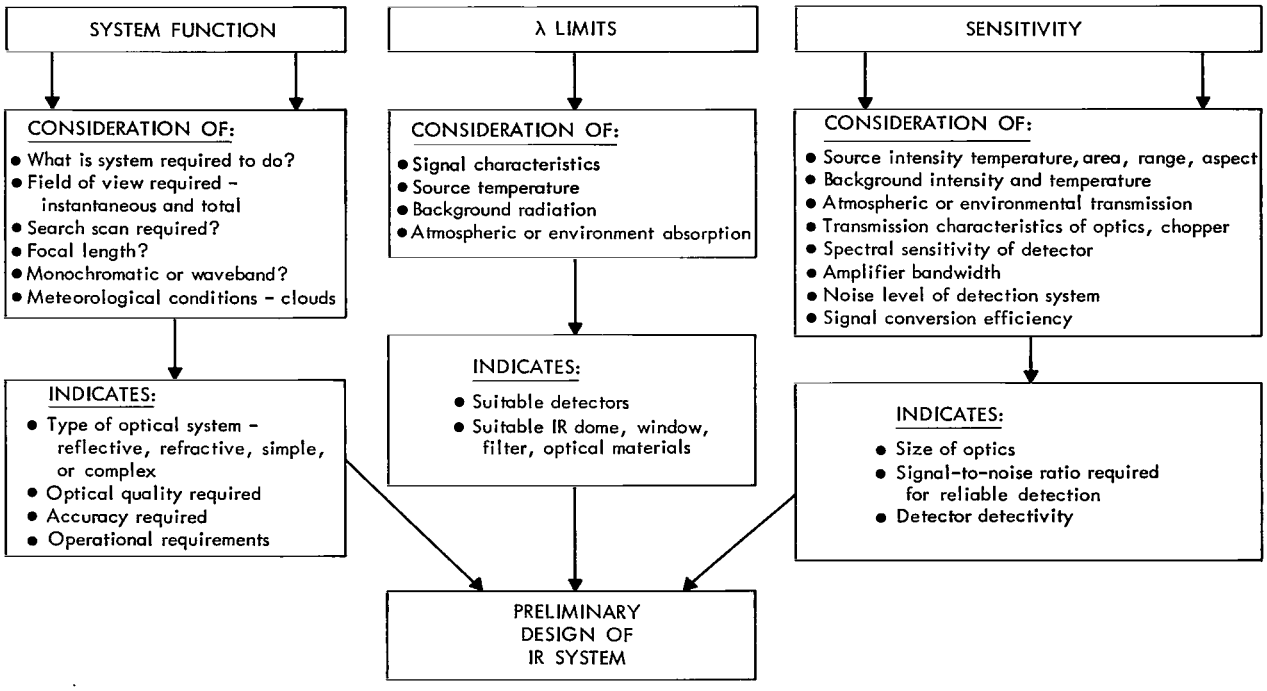

Figure 3—Preliminary design considerations (adapted from H. L. Hackforth, "Infrared Radiation," McGraw-Hill Book Company, Inc., New York, 1960).

proceed to develop the sensor equipment to optimally work with the energy available considering atmospheric and background effects, detector sensor characteristics, range and resolution requirements, and mission and operational requirements. These considerations are set forth in the form of a functional block diagram in Figure 3. This diagram depicts the processes and series of events which must be taken into account, in the order in which they occur.

A PERT diagram was developed for the Apollo IRATS project giving a conceptual picture of the events in chronological order and tasks which had to be accomplished for the effective procurement, design, construction, test and operational usage of the infrared reentry acquisition and tracking equipment.

SOURCE RADIATION CHARACTERISTICS

No direct spectral measurements have been made of a vehicle reentering the earth's atmosphere at super-orbital velocities, except for the recent Project Fire reentry. The results however are somewhat inconclusive as far as defining the spectral profile of the vehicle is concerned.

Nevertheless, many laboratory experimental data have been obtained and sufficient theory has been generated so that a fairly good prediction of the reentry radiation can be made. A notable example of the theoretical and supporting experimental work is that carried on at Ames Research Center by Craig and Davey (Reference 3) and Page and Arnold (Reference 4). To simulate the high reentry velocities, the Ames hypersonic free-flight facilities were used.

A typical plot of the spectral radiant emission characteristics versus wavelength of Lexan at high reentry velocities is shown in Figure 4. Lexan is a polycarbonate type of heat shield material with characteristics similar to the Apollo heat shield ablative material.

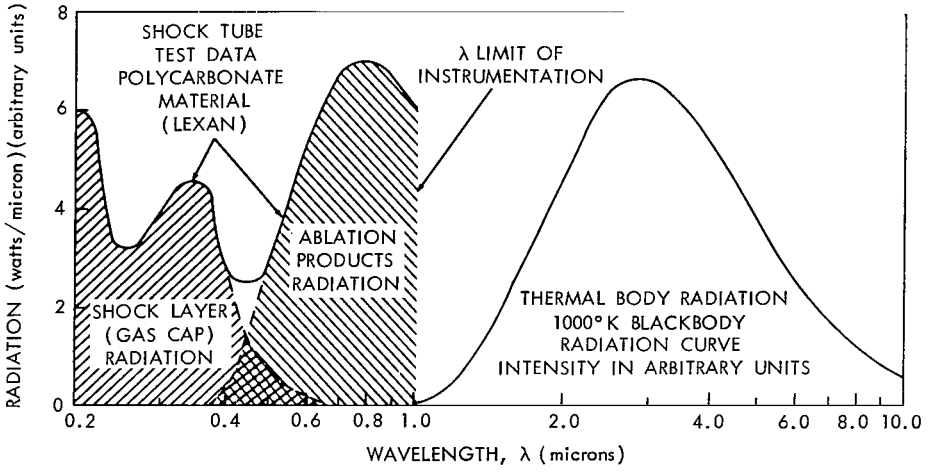

Figure 4—Typical radiant emission characteristics for a spacecraft reentering the earth's atmosphere at hypervelocity speeds.

The test results on other materials such as aluminum, polyethylene, and GE124 are reported and shown in Figure 5 (References 4 and 5). In every case the polycarbonate material exhibited a higher ablation product radiation than did the other three materials. The experimental results at Ames have shown that radiant energy below 0.5 micron is predominately from the shock layer, the region in front of the blunt face vehicle. Energy at wavelengths longer than 0.5 micron is predominately ablation products radiation in the region starting at the edges of the blunt face and proceeding back to form the wake of the reentry vehicle as shown in Figure 6.

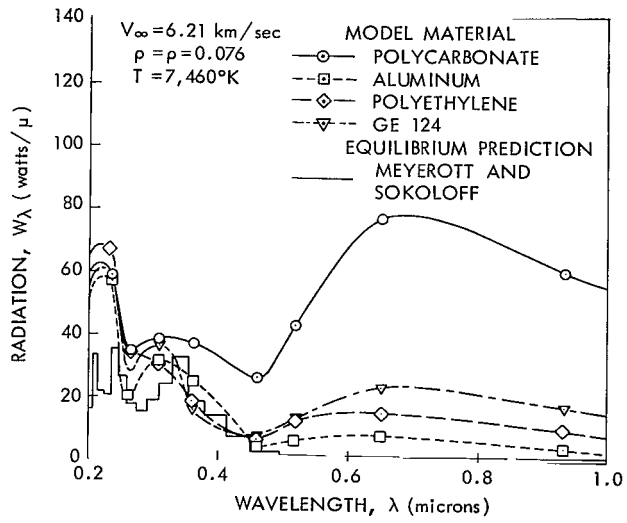

Figure 5—Radiant emission characteristics of different heat shield materials (from Reference 4).

Instrumentation used did not measure radiation above 1.0 micron. It therefore remains to predict the ablation products radiation above 1.0 micron and also the thermal blackbody radiation (infrared) resulting from vehicular heating. This effect can be drawn in as was done in Figure 4, thereby providing essentially the total spectral profile of a reentry vehicle.

Detection Wavelength Considerations

There are several good reasons for considering only the thermal body radiation and not the shock layer or ablation products radiation as the means for acquiring and tracking the Apollo vehicle during reentry.

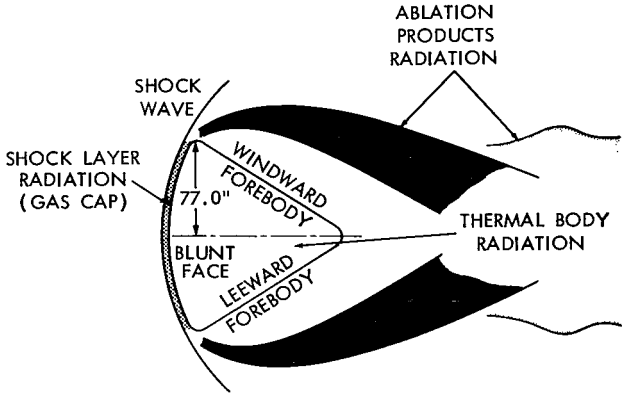

Figure 6—Apollo Command Module radiation regions.

The shock layer (ultraviolet) radiation is seriously attenuated by the atmosphere and since the Apollo mission is planned for a daylight reentry, the ultraviolet as well as the visible and near infrared would be difficult to detect in the presence of sunlit sky background.

A tracking system responsive to the thermal body radiation (middle infrared) would permit detection early in the reentry cycle. Also, during any skip period when there is less ultraviolet or visible radiation, acquisition and tracking would still be possible on the heated spacecraft. For clarification the following approximate waveband definitions are set forth: Ultraviolet - from 1×10^{-4} to 0.4 micron; visible - from 0.4 to 0.7 micron; near-infrared - from 0.7 to 2.7 microns; middle infrared - from 3 to 5 microns; and far infrared - from 8 to 13 microns.

The radiation from the spacecraft (thermal body) is fairly predictable, when one knows the surface material composition and the expected heat rate inputs. An extensive amount of theoretical and experimental work has been done on the thermodynamic effects to the spacecraft. In fact, this is one area that had to be extensively investigated before design could proceed on the Apollo Command Module. Not so predictable is the ultraviolet, visible, or near-infrared radiation (shock layer and ablation products) which, of course, varies with altitude, reentry angle, velocity, trajectory, range, etc. Also, experimental data indicate more scattering of radiation at shorter wavelengths. In addition, the daylight sky background radiation which one would have to contend with by working in the ultraviolet, visible, or near infrared is unpredictable. Data on atmospheric sky background however show a noticeable dip in intensity at approximately four microns (Figure 7).

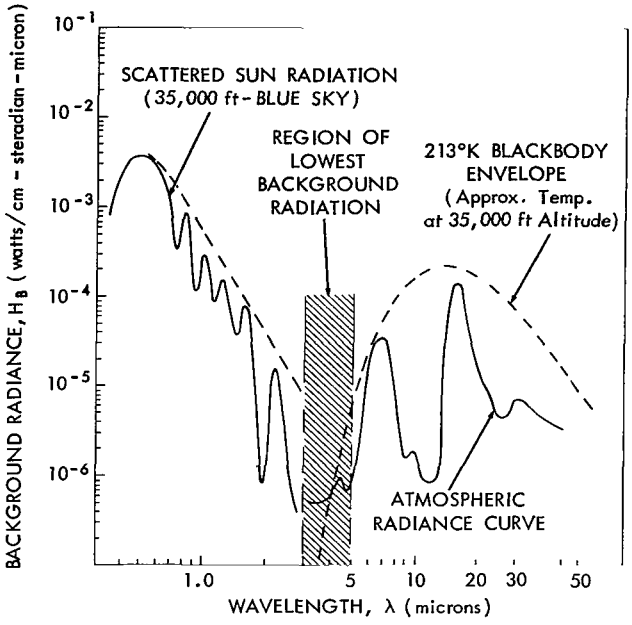

Figure 7—Typical atmospheric background radiance.

Also to be considered is the fact that use of a system responsive only to the middle IR reduces the sun impingement problem by a factor of approximately 20. The end result is having less of a "dead zone" as the system scans across the sun. There would also be less false target signals from stars or other extraterrestrial sources.

Infrared Radiation

Although experimental and theoretical work has proceeded quite far in defining the radiation characteristics of a super-orbital reentry vehicle, predicting the full scale infrared radiation from the heated surface of the Apollo spacecraft during reentry remains a problem. A study was therefore undertaken to define the boundary values for the maximum and minimum infrared radiation that the Apollo vehicle could generate (Reference 6).

Although the final design will consider such factors as area of the source and aspect angles, in the following analysis only maximum and minimum temperatures will be estimated. It will be shown that the temperature of the object lies between two values: a minimum temperature approximately equal to the ablation temperature of the material of the heat shield (assumed to be 1000°K) and a maximum temperature approximately equal to the equilibrium temperature of the spacecraft at the stagnation point (2500°K).

The boundary values are established by making certain idealistic assumptions about the Apollo vehicle surface material. The maximum value is obtained by assuming a perfect radiative heat

shield wherein all heat inputs are completely absorbed and radiated out. It is assumed that no heat is conducted into the vehicle and that the shield has no thermal capacity. These conditions result in an equilibrium temperature which is quite high and constitutes the hottest target possible.

The temperature at which the spacecraft reaches equilibrium is determined by calculating the rate of heat transfer to the spacecraft in the stagnation region as a result of both friction with air molecules and radiation of heated air within the shock wave. The total of these values results in an equivalent temperature of the spacecraft, which is assumed to radiate as a blackbody at the equivalent temperature.

The minimum value is obtained by assuming a perfect ablative heat shield wherein all heat inputs are absorbed until the surface reaches 1000°K, at which time the material ablates, trading mass for thermal energy with no further increase in surface temperature and no reradiation by the ablative products. Thus, the temperature of the minimum target would not exceed 1000°K.

Of course, neither of these idealistic heat shields exists in theory or practice but they do represent limiting characteristics of the ablative process.

Figure 6 illustrates the conditions existing during ablative reentry. A shock layer of definite thickness is formed in front of the leading surface of the spacecraft as the material of the heat shield ablating product is transferred into a wake around the spacecraft.

As the Apollo vehicle enters the atmosphere, the heating process commences and the surface temperature rises. When it reaches ablation temperature, further heat inputs are absorbed in changing the state of the ablation matter, say from solid to gas, which in turn is ejected into the boundary layer and carried away. If this process was ideal, the surface would remain at the ablation temperature. However, it is not ideal, as the ablation temperature varies with reentry conditions and the ablation products injected into the boundary layer reradiate at temperatures ranging from the ablation temperature to the stagnation temperature. Consequently, the infrared radiation can be expected to exceed that based on the ablation temperature alone once the ablation temperature is reached. As the ablation process proceeds, the ablative material recedes from the surface, leaving behind a char. This char acts as a radiative heat shield in that it has low thermal capacity and poor thermal conductivity. Consequently, the char surface becomes hotter than the ablation temperature and radiates away some of the heat input. It is obvious that the equilibrium temperature of the char will not reach that of the ideal radiative heat shield because some of the heat input is absorbed in the ablation process. Consequently, the infrared radiation can be expected to be less than that based on the equilibrium temperature of an ideal radiative heat shield.

The following analysis, therefore, endeavors to calculate the total heat input due to convective and radiative processes and from this to determine the equilibrium temperature. The equilibrium and ablation temperatures are then used to compute the boundary infrared radiation limits. The ablation radiation is calculated from extrapolated shock tube test data and represents the probable infrared radiation value. The shock wave is evaluated for its contribution to the infrared radiation and is merely added to the above values. All calculations are based on stagnation point conditions for the Apollo size vehicle.

Convective Heating

Convective heating is due to direct contact of the vehicle with air molecules. Little (Reference 7) cites a number of methods for calculating laminar stagnation point convective heating and points out that most are too unwieldy for approximate heating analyses. He gives as a noteworthy exception the approximation of Lees (Reference 8) which has been found to produce results close to the numerical mean of all methods considered for dissociating gases:

$$\dot{q}_c = 23.6\sqrt{\frac{P_\infty}{R_o}}\, u_\infty^3 \times 10^{-9} \text{ w/cm}^2 \quad , \tag{1}$$

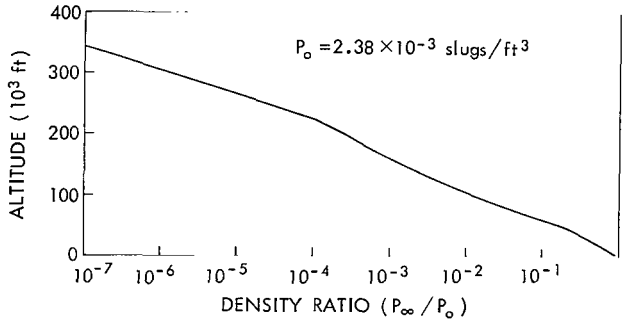

Figure 8—1959 ARDC standard atmospheric density.

where

$\dot{q}_c$ = laminar stagnation point convective heating rate in w/cm^2;

P_∞ = free-stream density in slugs/ft^3 (ratio P_∞/P_o based on the 1959 ARDC standard atmosphere is plotted in Figure 8),

R_o = axial radius ($\approx$6.5 ft) of the spacecraft at the heat shield (see Figure 6), and

u_∞ = velocity in ft/sec.

This equation was used for calculating the laminar stagnation point convective heating rates for the Apollo size reentry vehicle, and the results are plotted in Figure 9 as a function of altitude and velocity so that the heating rates for any reentry trajectory may be obtained directly.

A sample calculation is given below.

Given: altitude = 200,000 ft,

velocity = 30,000 ft/sec,

R_o = 6.5 ft, and

P_∞ = 5.95×10^{-7} slug/ft^3. This is derived by reading from the curve of Figure 8 as follows:

$P_\infty = (P_\infty/P_o) \times P_o$, where P_o is the sea level density

$= 2.5\times10^{-4} \times 2.38\times10^{-3}$

$= 5.95\times10^{-7}$ slug/ft^3.

Substituting these values in Equation 1,

$$\dot{q} = 23.6\sqrt{\frac{5.95\times10^{-7}}{6.5}} \times (3\times10^4)^3\times10^{-9} = 193 \text{ w/cm}^2 \quad .$$

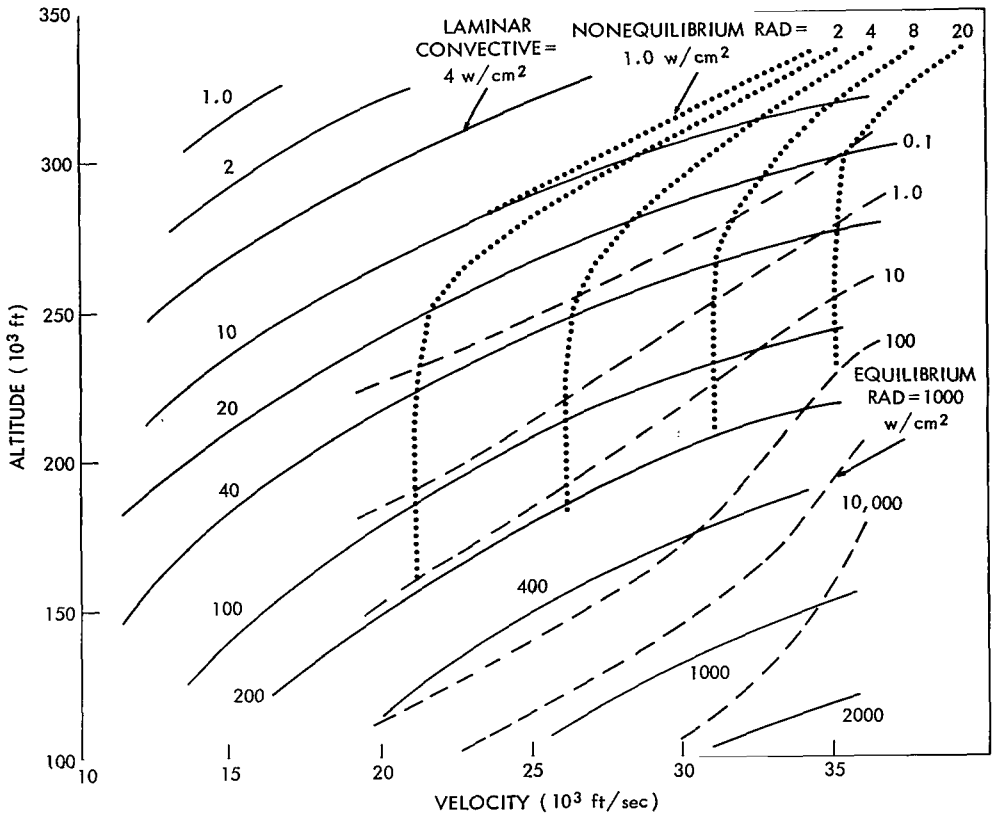

Figure 9—Apollo type reentry stagnation point heating rates.

Radiative Heating

Figure 10 shows that the reentering Apollo vehicle will encounter high shock layer temperatures. Thus, the emissivity of heated air becomes significant, making radiative heating from the shock layer an important contributor.

There is a finite time for gas to react chemically to changes in temperature which, although small, is sometimes significant when compared with the time required for gas particles to move through the shock layer of a hypervelocity vehicle. This reaction zone, referred to as a region of nonequilibrium, constitutes a transition period between air at atmospheric temperature and density and air at shock layer temperature and density equilibrium, and thus exists at the forefront of all hypersonic shock waves.

Page (Reference 5) refers to two distances into the forefront of the shock layer (δ_e, the excitation distance, and δ_r, the relaxation distance) which describe the depth of the nonequilibrium state. Page describes a model of this state wherein a temperature overshoot at δ_e exists, resulting in the integral of radiation taken over the distance δ_r being larger than the radiation from an equivalent depth of equilibrium shock layer. Further, his model indicates that the integral of radiation taken over the distance δ_r is a constant independent of density.

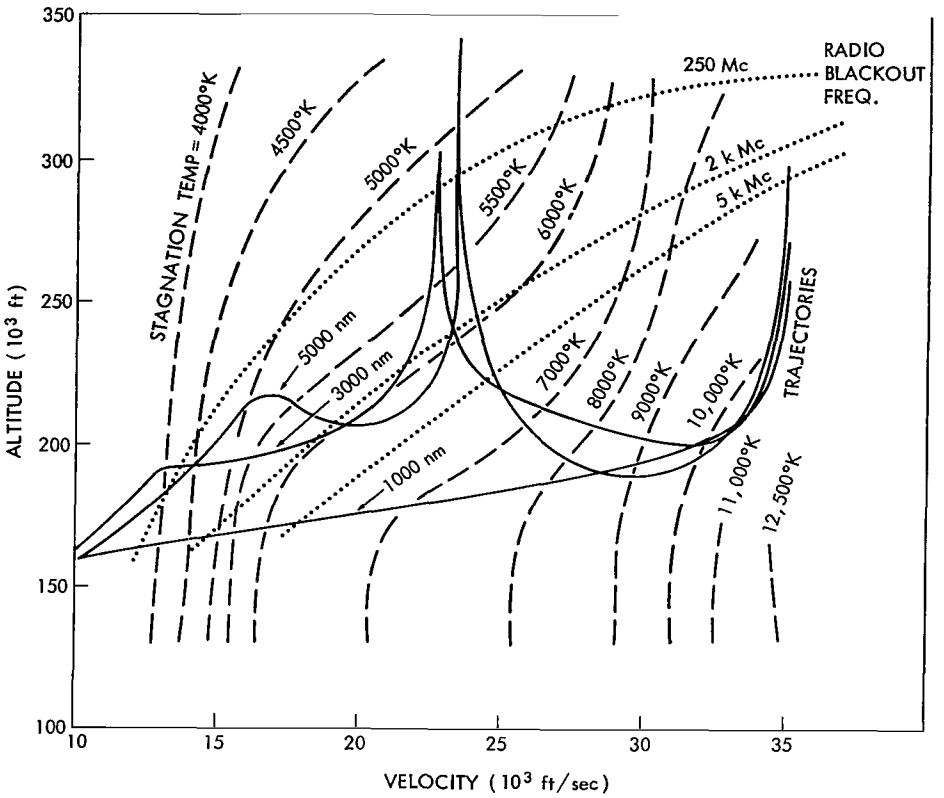

Figure 10—Apollo reentry vehicle profiles (from Reference 1).

Both results are pertinent to any radiative heating analysis, as may be better understood from the following relations. Figure 11 illustrates the temperature transition phenomenon described above. The depth of the shock layer is designated by δ_s and approximated by Page as

$$\delta_s = \frac{3R_o}{4P/P_\infty} . \tag{2}$$

It can be seen that δ_s increases with density and size of the vehicle. Inasmuch as the equilibrium radiation is proportional to this depth, it will likewise increase with density and vehicle size. The nonequilibrium radiation in Page's model, however, is fixed and independent of both these factors so long as $\delta_s \gg \delta_r$. Consequently, if the density and size are such that $\delta_s \gg \delta_r$, then the equilibrium radiation will constitute the principal source of radiation heating. If, on the other hand, these factors are such that δ_s approaches δ_r, then the nonequilibrium radiation will constitute the principal radiative heating source.

Any excited air which passes completely through the shock layer is expected to be quickly quenched. Therefore, if the flow time from the shock to the stagnation point is less than the relaxation time, the nonequilibrium radiation will be significantly reduced. This effect is called truncation.

In general, as a hypersonic velocity vehicle enters the atmosphere, one can expect a nonequilibrium component of radiation to develop which will be an increasing function of density until such a density is reached that the shock layer thickness, δ_s, greatly exceeds the relaxation distance, δ_r. This nonequilibrium component of radiation will then remain constant for all further density increases. However, as the density continues to increase with continual descent in altitude, the shock wave thickness, δ_s, will approach a value where the equilibrium radiation equals the nonequilibrium value. Up to the time that this density is approached, the nonequilibrium component of radiation comprises the major source of radiative heating. From this density on to increasing values the equilibrium radiation will continue to increase, becoming the dominant radiative heating source. The magnitude of equilibrium radiation will be an increasing function of vehicle velocity and size. The magnitude of the nonequilibrium component will also be an increasing function of velocity but independent of vehicle size. However, the altitude or density at which the nonequilibrium component reaches full maturity will be a function of vehicle size, since the shock standoff distance is proportional to vehicle size.

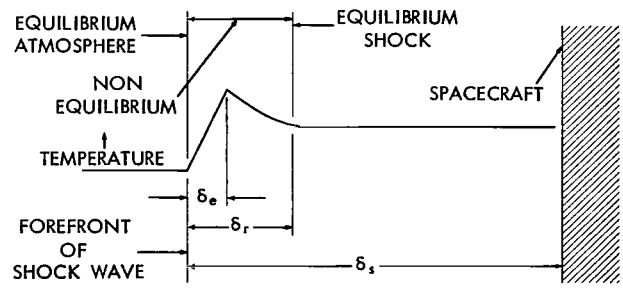

Figure 11—Shock layer temperature transition.

Equilibrium Radiation

Kivel (Reference 9) presents data on the equilibrium radiation of hot air. Figure 12 taken from Reference 10 gives the amount of radiation toward a body per cubic centimeter of air as a function of velocity and altitude. Also given is the stagnation point density ratio.

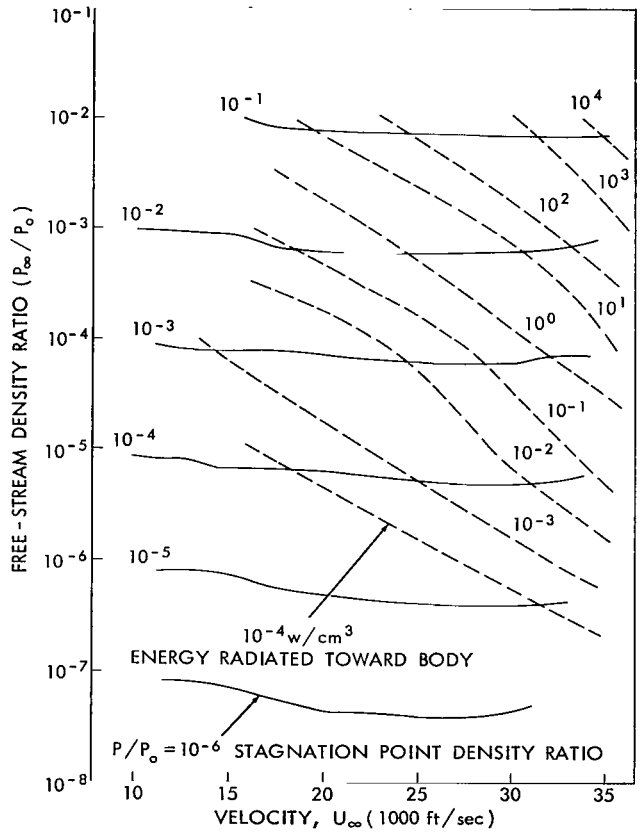

Figure 12—Equilibrium radiation.

The equilibrium radiation heat rate is computed by selecting the radiation value per cubic centimeter from Figure 12 and multiplying this by the shock wave depth as determined from Equation 2. These results are also plotted in Figure 9.

A sample calculation is given below.

Given: altitude = 200,000 ft,

velocity = 30,000 ft/sec,

R_o = 6.5 ft.

The free-stream density ratio corresponding to the given altitude is obtained from Figure 8.

$$P_\infty/P_0 = 2.5\times10^{-4} .$$

The stagnation point density ratio corresponding to this free-stream density ratio and the given velocity is obtained from Figure 12.

$$P/P_o = 4\times10^{-3} .$$

The ratio of stagnation point density to free-stream density is then

$$P/P_\infty = \frac{P}{P_o} \times \frac{P_o}{P_\infty} = \frac{4\times10^{-3}}{2.5\times10^{-4}} = 16 .$$

Inserting this ratio and R_o (6.5 ft = 198 cm) into Equation 2 yields the shock thickness:

$$\delta_s = \frac{0.75\times198}{16} = 9.3 \text{ cm} .$$

The energy radiated toward the body for the given altitude and velocity is obtained from Figure 12 and is seen to be approximately 3 watts/cm^3. Multiplying this value by the shock layer thickness yields the stagnation point equilibrium radiation heating rate, $\dot{q}_r$

$$\dot{q}_r = 3\times9.3 = 28 \text{ w/cm}^2 .$$

Nonequilibrium Radiation

Page (Reference 5) has obtained measurements of total radiation for several velocities as a function of free-stream density. As a result, he was able to determine the free-stream density associated with each velocity at which the shock standoff distance just equaled the nonequilibrium relaxation distance, and consequently, the magnitude of the nonequilibrium radiation.

His measured data are shown by the solid curves in Figure 13. The dashed lines in Figure 13 are the predicted equilibrium radiation values. The difference between the measured total radiation and the predicted equilibrium radiation gives the nonequilibrium component.

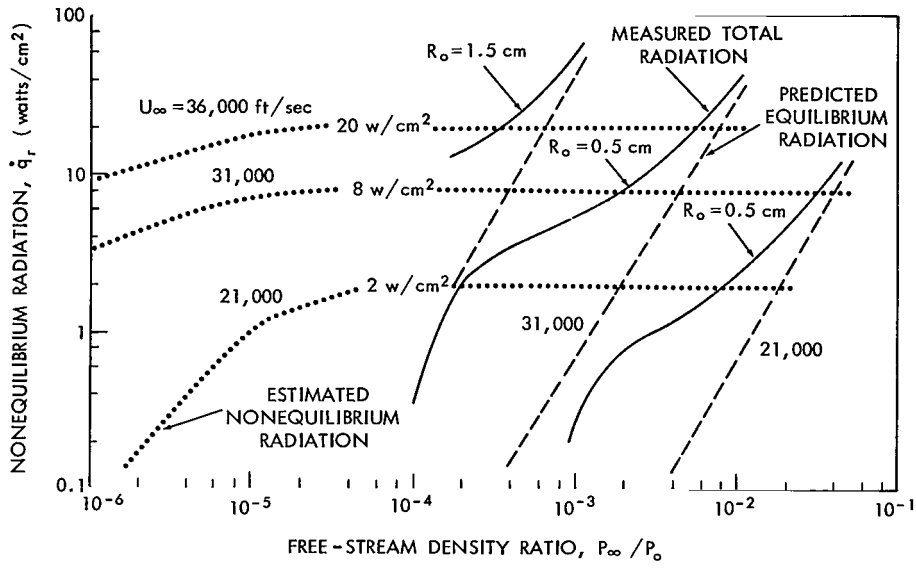

Figure 13—Nonequilibrium radiation.

In accordance with Page's theory discussed earlier, this nonequilibrium component remains constant at any given velocity and is not a function of body size, except for truncation effects. The width of the nonequilibrium zone is proportional to density and the shock width is proportional to nose radius. Therefore, to determine the density at which the nonequilibrium component develops in the Apollo case, it is necessary to translate Page's nonequilibrium measurements by the ratio of the model nose radius to the Apollo vehicle nose radius. These results are shown as the dotted curves in Figure 13.

Using these curves as a basis, extrapolations of nonequilibrium radiation as a function of velocity and altitude are obtained and plotted in Figure 9. A sample calculation for the model is given below.

Given: $R_o = 0.5$ cm,

$U_\infty = 31{,}000$ ft/sec, and

$P_\infty/P_o = 2\times10^{-3}$.

The total radiation measured by Page shown in the solid curve of Figure 13 for these conditions is

$$I_T = 8 \text{ w/cm}^2 .$$

The predicted component of equilibrium radiation from the dashed curve of Figure 13 is

$$I_e = 2 \text{ w/cm}^2 .$$

Therefore, the nonequilibrium component (I_n) is

$$I_n = I_T - I_e = 6\ \text{w/cm}^2 .$$

Now the Apollo vehicle nose radius is approximately 200 cm while the model radius is only 0.5 cm. Therefore, the density at which this 6 w/cm^2 value of nonequilibrium radiation would be obtained in the Apollo case is 400 times lower than the given density, or

$$P_\infty/P_{o(\text{Apollo})} = 2\times10^{-3} \times \frac{0.5}{200} = 5\times10^{-6} .$$

Hence, 6 w/cm^2 is plotted at this density in the dotted curve.

Conclusions on Surface Radiation Limits

The boundary values of surface emission may now be obtained. The reentry trajectory is first superimposed on Figure 9 and the total heat inputs are summed up for every point on the trajectory. The equilibrium temperature is then determined by solving Planck's blackbody equation.

$$T_{eq} = \sqrt[4]{\frac{q\ \text{total}}{\sigma_\epsilon}}\ ^\circ\text{K} .$$

A sample calculation is given below for the maximum heating conditions.

Given: altitude = 200,000 ft and

velocity = 30,000 ft/sec.

From Figure 9 the input heat rates are:

	convective	$\dot{q}_c = 193$ w/cm^2,
radiative	equilibrium	$\dot{q}_e = 28$ w/cm^2,
radiative	nonequilibrium	$\dot{q}_n = 7.5$ w/cm^2, and
	total	$\dot{q}_T = 228.5$ w/cm^2.

The equilibrium temperature from Equation 3 is then

$$T_{eq} = \sqrt[4]{\frac{228.5}{5.7\times10^{-12}}} = 2500^\circ\text{K} .$$

The temperature of the reentering spacecraft during ablative reentry will lie between 1000°K and 2500°K.

ATMOSPHERIC TRANSMISSION AND BACKGROUND RADIATION

Atmospheric Transmission

A number of different atmospheric constituents act to attenuate an infrared signal as it passes through the atmosphere from the source to the receiving apparatus. The effect of the earth's atmosphere must therefore be considered in the analyses of the capability of infrared sensing equipment.

The atmosphere is composed of a mixture of gases in which are suspended a wide variety of particles distributed over a great range in size and differing in chemical composition. These gases cause radiation to be absorbed and the suspended particles scatter the radiation.

The gases present in greatest abundance in the earth's atmosphere (Reference 11) are nitrogen, oxygen, water vapor, carbon dioxide, methane, nitrous oxide, carbon monoxide, and ozone. Fortunately, the two gases present at the highest concentrations, N_2 and O_2, are homonuclear. They, therefore, possess neither a permanent nor an induced electric moment and hence do not exhibit molecular absorption bands.

Over the range of altitudes extending from sea level to approximately 40,000 feet, water vapor and carbon dioxide are by far the most important absorbing molecules. The concentration of H_2O varies between 10^{-3} percent and 1 percent (by volume), depending upon geographical location, altitude, time of year, and local meteorological conditions. Carbon dioxide, CO_2, is much more uniformly distributed; it varies between 0.03 and 0.04 percent and is greater in an air mass which has been over heavy vegetation than in the atmosphere over the ocean. The distribution is more uniform at higher altitudes where the mixing is more complete. Methane, CH_4, is present at a concentration between 1×10^{-4} and 2×10^{-4} percent and is very uniformly distributed in altitude. Nitrous oxide, N_2O, at concentrations of 3×10^{-5} to 4×10^{-5} percent, and carbon monoxide, CO, with a typical concentration of 2×10^{-5} percent, have bands which show up if long paths are utilized. Ozone, O_3, is present at concentrations as large as 10^{-3} percent at altitudes near 100,000 feet, but at much lower concentrations at other altitudes.

The atmospheric transmission was calculated by using the procedures established by Altshuler (Reference 12). He considers a model consisting of infrared absorbing atmospheric constituents (CO_2, O_3, N_2O, CH_4, CO, and water vapor) and their variation in accordance with temperature and pressure changes with altitude based upon the 1959 ARDC model atmosphere. He also takes into account the earth's curvature and refraction of infrared in the earth's atmosphere.

Consideration of the relative distribution with altitude above 40,000 feet of the CO_2 and water vapor absorbers as derived from Altshuler indicates that the bulk of the absorber exists below 100,000 feet. Therefore, the absorbing atmosphere was considered to exist only to an altitude of 100,000 feet. It is then sufficient to calculate the atmospheric transmission between the altitudes of 40,000 and 100,000 feet as a function of look angle from 0 to 90 degrees and apply the results directly to the Apollo case, regardless of the Apollo vehicle altitude.

Based on the above considerations, Altshuler's procedures were used to calculate the spectral transmission of the atmosphere out to a wavelength of 3.5 microns as a function of look angle from 0 to 90 degrees from a 40,000 foot platform (Figure 14).

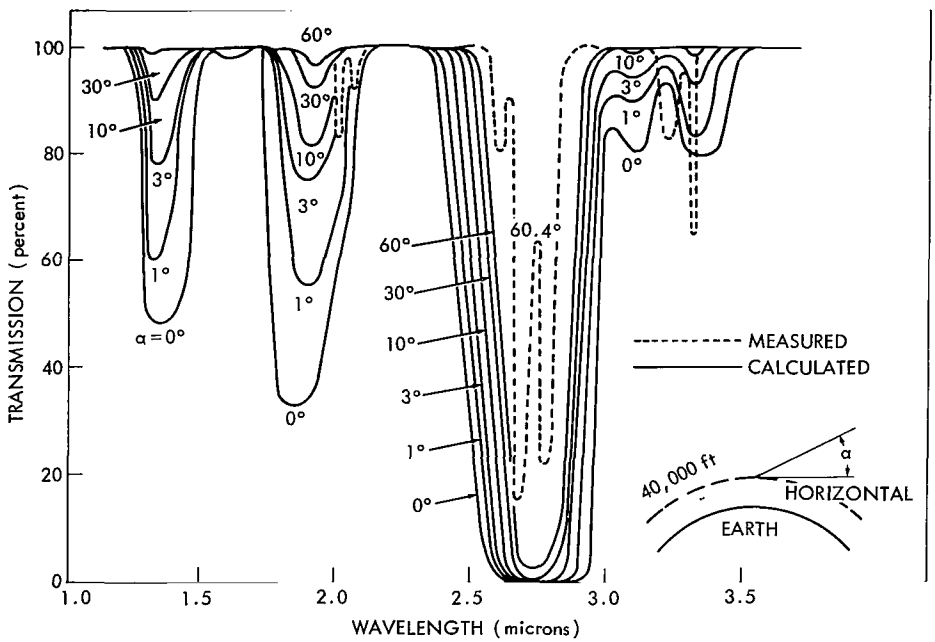

Figure 14—Atmospheric transmission.

To check the validity of these results to the actual case, the calculated results were compared with experimental measurements. Murcray (Reference 13) has made measurements with a balloon of the atmospheric transmission as a function of altitude. A set of his data obtained at 40,000 feet with a look angle of 60.5 degrees is also shown in Figure 14. Although his data show a higher resolution, they are in good agreement with the calculated curves of Figure 14 and one can therefore conclude that these curves are both realistic and applicable.

It remains then to calculate the atmospheric transmission out to a wavelength of 5 microns to cover the 3 to 5 micron band where transmission is high, however, there is no reason to believe that with the above considerations and using Altshuler's procedures, the calculations would not be in good agreement with actual measured conditions.

Cloud Cover Analysis

Of direct concern, obviously, is the cloud coverage over the expected Apollo reentry area. Clouds between the search aircraft flying at 35,000 feet and the target would seriously attenuate the signal received by any optical sensing device. The Space Flight Meteorological Group, U. S. Weather Bureau has undertaken a study, based on data compiled over several years, of the cloud

cover problem over the Apollo reentry area encompassing 18 million square miles in the Western Pacific. The results of this study are presented in Appendix A. Briefly, the average results show that there would be clear skies above the aircraft 90 percent of the time for 45 percent of the area, 50 to 90 percent of the time for 50 percent of the area, and less than 50 percent for 5 percent of the area.

It is interesting to note that the area of high cloudiness is a result of the inter-tropical convergence zone which is a rather well defined area. In fact, if one would station an aircraft fifty miles from a cloud top which reached 50,000 feet, viewing would still be possible down to less than three degrees above the horizon. It should also be borne in mind that eight aircraft would be deployed to cover the reentry trajectory so that if the field of view of one infrared system was obscured by clouds it is highly unlikely that the other systems, situated hundreds of miles apart, would be (Reference 1). Also, if the field of view of any one of the infrared systems were partially obscured by clouds so that there were clear spaces between the clouds, continuous spacecraft tracking would still be possible across the sky because of the memory track capability built into the system. It was therefore concluded from the report that the Apollo operational requirements could be met by the infrared systems operating on highly mobile aircraft flying at high altitudes.

Background Radiation

The infrared system must acquire the target source radiation while discriminating against other sources of radiation within the field of view of the infrared system. Since all objects at temperatures above absolute zero emit energy in the infrared, the background radiation is always present and thus competes with the target source radiation. It is therefore necessary to consider the characteristics of the background radiation in the effective analysis of any infrared system.

Competing background radiation can exist in many forms. Background radiation from the sky is caused by scattered sunlight from water droplets, molecules, and other particles suspended in the atmosphere and from the thermal emission of the atmospheric constituents themselves.

Extraterrestrial sources such as the sun, moon, stars, and planets contribute to the overall sky background radiation. However, the larger effect, except for the sun, is one of appearing as false targets, or, as in the case of the sun, of limiting the usefulness of the scanner as the infrared system scans across it.

Radiation associated with the instrumentation platform (a multijet aircraft) and the instrument itself has to be considered. Sources of this radiation include the jet engine exhausts, aircraft appendages such as the vertical stabilizer which could reflect and radiate energy into the infrared receiver, and heating of the optics from the friction of the high speed air moving over the optics.

Another "false target" worth mentioning is the Apollo Service Module which could be reentering the earth's atmosphere at about the same time and in near proximity to the real target—the Apollo Command Module.

Although various false targets must be taken into account, they are not considered a serious problem since discrimination circuitry is available to cancel background signals and also the operator can exercise a good deal of judgment in choosing the real target - the Apollo command module - from the relative velocity of the target with respect to the background and from the trace on the operator's screen.

Sky Background

The radiation from a clear sky results mainly from two sources:

1. the scattering of the radiation from the sun and
2. the thermal emission from the constituents of the atmosphere.

The sun radiates nearly as a 6000°K blackbody and is radiating approximately 3×10^{3} watt/cm^{2} -μ - ster. Measured on the earth's surface the clear sky radiance is approximately 3×10^{-3} watts/ cm - μ - ster at 0.5 micron. An exact measurement of the scattered sunlight in the waveband of interest and at the desired altitude would necessarily have to take into account the meteorological conditions and the position of the sun with reference to the infrared equipment. Sky maps showing lines of constant radiance in the 0.6-2μ region taken at Pikes Peak (elevation 14,000) (Reference 14) are shown in Figure 15. The referenced article also presents sky radiance maps taken at 1000 and 6000 feet as a comparison. The variation of sky radiance is apparent and is to be expected as the infrared system scans the hemisphere. This variation in intensity would give rise to a low frequency signal which, if large enough, could cause limiting in the infrared system preamplifier circuitry. Less variation is to be expected at the higher aircraft altitude of 35,000 feet.

As to be expected at the longer wavelengths, the scattered sunlight is less because of the reduced intensity of the sun's radiation at the longer wavelengths. At above 4 microns, the atmospheric thermal emission is predominant and the scattered sunlight can be neglected for most

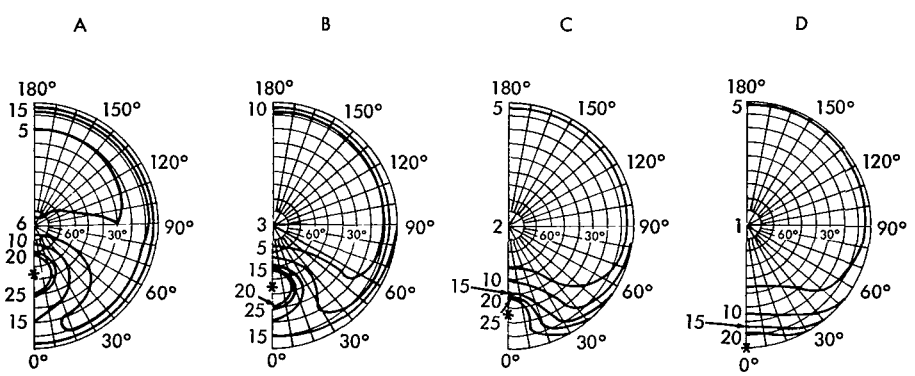

Figure 15—Sky maps showing lines of constant radiance in w/(m^{2}-sterad) in the 0.6-2μ wavelength region at Pikes Peak, September 15. The data were taken at: A, 12:05 P.M., sun elev. 54°; B, 2:06 P.M., sun elev. 43°; C, 3:47 P.M., sun elev. 27°; and D, 6:05 P.M., sun elev. 0° (from Reference 14).

practical purposes. In fact, it has been found experimentally that under nearly all conditions, the atmospheric emission and scattered sunlight are equal in the 3 to 4 micron range. Measurements taken at high altitude (30,000 to 40,000 feet) show this to be true but over a broader range extending to 5 microns. Curves are presented from the measurements made by Bell et al. (Reference 15) and Jamieson et al. (Reference 16) in Figures 16 and 17. These curves are a measure of the clear sky thermal emission at Pikes Peak and Colorado Springs and of the clear sky sun scattered radiation and thermal emission measured at Colorado Springs, Colorado.

Celestial Background

Celestial background is not considered a problem in the middle and far infrared except for the sun and the moon. It is interesting, nevertheless, to look at the stellar irradiance in the infrared of several stars and compare this with the irradiance in the visible, the basis upon which the above conclusion can be drawn.

A notable piece of work done in this area is that by Walker and D'Agati (Reference 17) who have compiled data on seventy-one stars. The data are in the form of a table in absolute energy units and are for discrete wavelengths in the infrared region from 1.0 to 10.0 microns. Also given is the response at 0.566 microns for comparison.

It is not unreasonable to consider an infrared system with a sensitivity of 10^{-12} watt/cm^2. An examination of the table in the referenced material will reveal that at wavelengths longer than 2.5 microns there are very few stars with irradiance values greater than 10^{-12} watt/cm^2.

However, at wavelengths shorter than 2.5 microns and especially in the visible, there are many stars with energy levels greater than 10^{-12} watt/cm^2. These would be detected and show up as false targets on the operators screen. In fact, the ability to see stars in the daylight with small field-of-view star tracker systems is used for aerial navigation purposes.

Other infrared stellar measurement programs indicate the same result—the absence of sources of detectable

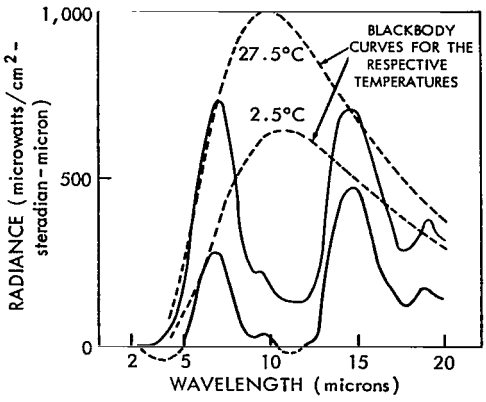

Figure 16—Clear zenith sky thermal emission measured at Pikes Peak, Col.; elevation 14,110 ft.; ambient temperature 2.5°C; and Colorado Springs, Col.; elevation 6000 ft.; ambient temperature 27.5°C. (By permission McGraw-Hill Book Company, Inc., New York [Reference 15].)

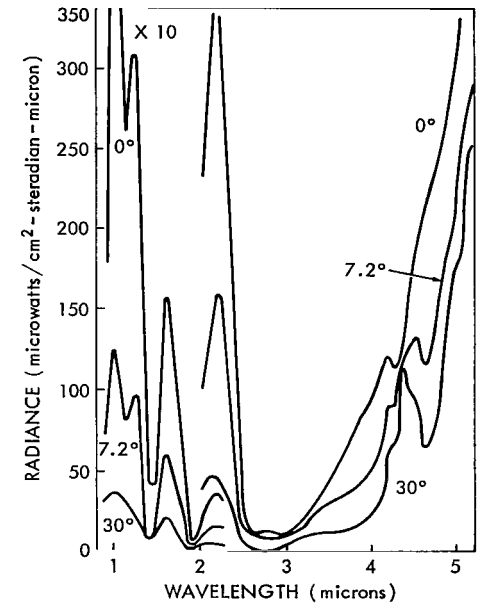

Figure 17—The spectral radiance of the clear noon sky as measured from Colorado Springs, Col. The elevation angles starting with the upper curve are 0°, 7.2°, and 30°. Note that the radiance values below about 2μ are ten times larger than the ordinate scale shown. (By permission McGraw-Hill Book Company, Inc., New York [Reference 16].)

intensity at the longer infrared wavelengths. For instance, the study by Hall (Reference 18) presents the results of an infrared stellar mapping program where measurements were made of the clear night sky in three spectral regions of the infrared.

Significant results were obtained only for the shorter wavelength region (1.3-3.0 microns). Figure 18 shows the relationship of the blackbody radiation curves for some celestial objects.

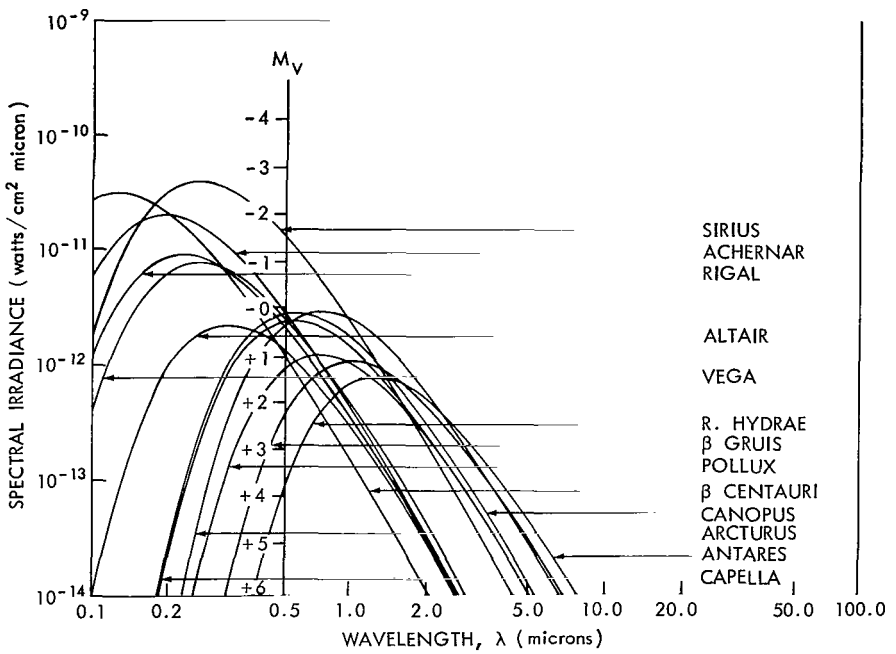

Figure 18—Spectral irradiance of bright stars.

Platform and Optics Radiation

The location of the scanner exterior to the aircraft subjects it to air friction heating and the vertical stabilizer which partially obscures the field-of-view of the infrared system also acts to reflect background radiation into the system (Figure 19).

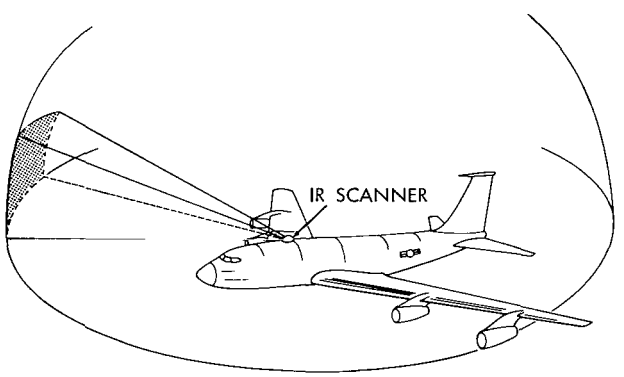

Figure 19—Location of infrared scanner on aircraft.

Radiation from the jet engines or exhaust is not considered a serious problem because of the location of the scanner on top of the aircraft fuselage and the limited downward scan angle.

In Figure 20 the stagnation temperature on an IR dome or optics is plotted against aircraft Mach number. It may be seen that at the expected aircraft altitude (30k to 40k feet) and at

a speed less than Mach 1 the temperature of the IR dome or optics is actually less than standard room temperatures. Therefore, no degradation in performance is expected; in fact, there should be a slight improvement.

Clouds

If clouds were not in the line of sight but still within the search field of the infrared equipment, they could reflect sufficient sunlight to appear as a target on the operator's screen. However, as noted above, there are adequate means for choosing the real target.

SYSTEM DESIGN CONSIDERATIONS

The mission support requirements for the infrared system (Reference 1) are such that it should have the capability of searching out the total hemisphere and acquiring, locking onto and tracking the target, thereby generating angle coordinate information for pointing other communication antennas, derivation and recording of the Apollo reentry trajectory, and impact point prediction.

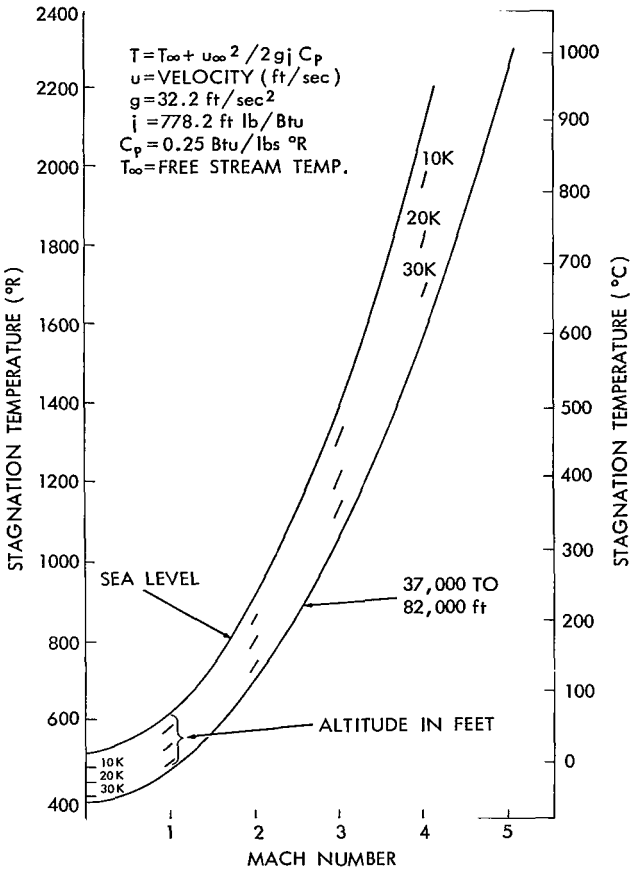

Figure 20—IR Dome stagnation temperature vs. Mach number.

The angular rate of the Apollo vehicle with reference to the infrared system (Figure 21) requires that constraints be placed upon the time allowed to search out the hemisphere and associated "lock on" time, once the target has been identified. Since these constraints directly enter into the design of an infrared system in terms of dwell time, bandwidth, resolution, etc., an analysis of the problem is herein presented.

Hemispherical Search

The geometry of the problem is shown in Figure 22. The hemispheric search volume is truncated on the top at the altitude above which the Apollo vehicle cannot be detected because it has not reentered the atmosphere to generate sufficient radiation for detection and because the skip trajectory is not expected to exceed this altitude. Limiting the required range above this altitude limits the required dynamic range of the infrared system. For the analysis, however, a hemisphere is considered and the equations are derived on this basis.

Design Analysis

The design analysis proceeds by first deriving a general equation for calculating the sensitivity of an infrared search system, considering the geometry of the problem and other parameters involved. The equation is presented for calculating the irradiance at the receiver, appropriate range, and atmospheric transmission. Optical and detector parameters are inserted in the equations and a comparison is made between the irradiance at the receiver and the system sensitivity.

The geometry of the problem is presented in Figure 23, where

- A = total azimuth search field (radians),
- B = total elevation search field (radians),
- a = instantaneous azimuth field of view (radians),
- b = instantaneous elevation field of view (radians),
- D_o = entrance aperture diameter of collecting optics (cm),
- θ = angle of projected instantaneous field of view (radians),
- f_L = focal length of optics (cm),
- d_ω = width dimension of detector (cm) and
- d_ℓ = length dimension of detector (cm).

Assuming simple geometric optics, the detector area, A_d, can be equated in terms of the optical parameters and instantaneous field of view:

$$\tan\theta = \frac{d_\ell}{f_L} = \theta(\text{in radians}) . \qquad (3)$$

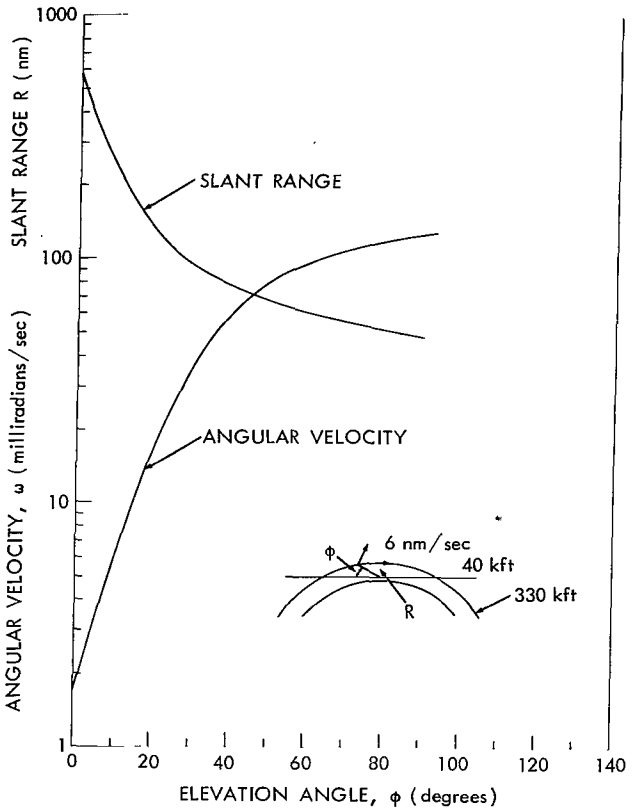

Figure 21—Angular velocity and slant range versus elevation angle of the IR tracker during Apollo reentry.

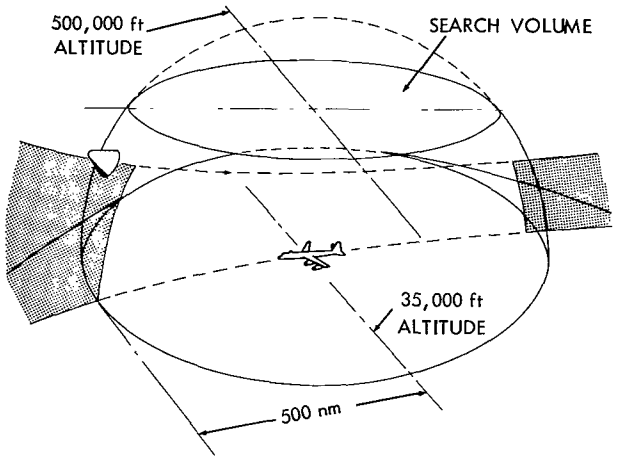

Figure 22—Apollo reentry—IR search volume.

A point detector is considered and the instantaneous field of view is small. For small angles, the tangent of the angle is equal to the angle in radians. Also, $f_L >> d_\ell$.

The optics f/ratio is defined as

$$f/\text{ratio} = F = \frac{f_L}{D_o} \quad . \tag{4}$$

Therefore Equation 3 can be rewritten as

$$d_\ell = FD_o\,\theta_\ell \quad . \tag{5}$$

Similarly,

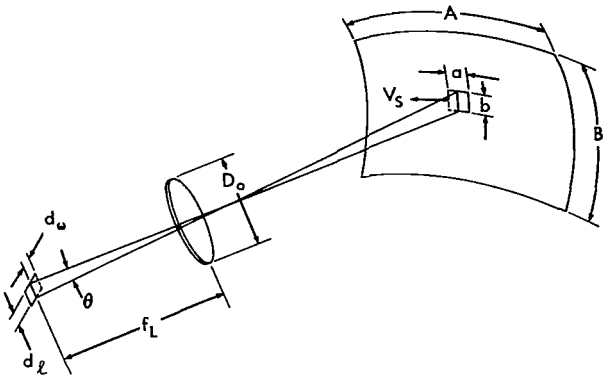

Figure 23—Search geometry.

$$d_\omega = FD_o\,\theta_\omega \quad . \tag{6}$$

Consequently, the detector area, A_d, may be expressed as

$$A_d = d_\ell\, d_\omega = (FD_o)^2\, ab \quad , \tag{7}$$

where from the geometry of the problem

$$ab = \theta^2 \text{ steradians} \quad . \tag{8}$$

If the search field is to be scanned in a frame time, T_f, then the search rate, S_r, scan velocity, V_s, and dwell time, T_d, may be derived from the geometry of Figure 23.

$$\text{Search rate, } S_r = \frac{AB}{T_f} \text{ steradians/second} \quad . \tag{9}$$

To determine the scan velocity, V_s, a line scan in the azimuth direction is considered. The width of the "line" is the instantaneous field of view in the elevation direction.

$$\text{Scan velocity, } V_s = \frac{\text{number of lines} \times \text{length per line}}{\text{frame time}}$$

$$= \frac{BA}{bT_f} = \frac{S_r}{b} \text{ radians/second} \quad . \tag{10}$$

$$\text{Dwell time, } T_d = \frac{a}{V_s} = \frac{ab}{S_r} = \frac{\theta^2}{S_r} \text{ seconds} \quad . \tag{11}$$

System Sensitivity

The system sensitivity is defined in terms of the noise equivalent flux density (NEFD) in watts/cm^2. This is the irradiance at the receiver aperture which will produce a signal from the detector which is just equal to the inherent noise of the detector.

The detector noise is often given in terms of the noise equivalent power (NEP) in watts. This is the amount of radiation falling on the detector which will produce a signal equal to the detector inherent noise level. This expression for the different detector noise processes always contains the factor $\sqrt{A\Delta f}$. Therefore, one can say that

$$NEP \propto \sqrt{A\Delta f} \quad . \tag{12}$$

Jones suggested that a quality, D*, be defined as

$$D^* = \frac{\sqrt{A_d\ \Delta f}}{NEP} \quad , \tag{13}$$

which serves to characterize the detector in terms of the intrinsic properties of the material of which it is made (Reference 19).

The noise equivalent flux density can now be defined in terms of the detector noise equivalent power, optical, and electronic parameters:

$$NEFD = \frac{NEP}{A_o\ \tau_o\ K} \quad , \tag{14}$$

where

A_o = total clear aperture area of optics,

τ_o = optical efficiency, and

K = conversion efficiency which includes the effects of the electronic filter, optical transfer characteristics, i.e., blur circle size, reticle function, etc.

The collecting area of the optics may be defined as

$$A_o = \frac{\pi D_o^2}{4}\ cm^2 \quad . \tag{15}$$

Substituting Equations 7 and 8 into 13 yields an expression of NEP in terms of the optical parameters.

$$NEP = \frac{FD_o\ \sqrt{\theta^2\ \Delta f}}{D^*}\ watts \quad . \tag{16}$$

Now Equations 15 and 16 may be substituted into Equation 14 to express NEFD in terms of the optical parameters:

$$NEFD = \frac{4F\sqrt{\theta^2 \Delta f}}{\pi D_o \tau_o KD^*} \text{ watts/cm}^2 . \quad (17)$$

Substituting Equations 11 in 17 yields NEFD in terms of dwell time and search rate,

$$NEFD = \frac{4F\sqrt{T_D S_r \Delta f}}{\pi D_o \tau_o KD^*} \text{ watts/cm}^2 . \quad (18)$$

The above equations have been derived on the basis of one detector element. However, if n detector elements are used, then, from Equation 10,

$$V_s = \frac{B}{nb} \frac{A}{T_f} \text{ radians/sec , and} \quad (19)$$

$$T_D = \frac{n\theta^2}{S_r} \text{ seconds} . \quad (20)$$

Substituting Equation 20 into 18 gives

$$NEFD = \frac{4F\sqrt{T_D S_r \left(n^{-1}\right) \Delta f}}{\pi D_o \tau_o KD^*} , \quad (21)$$

a general equation which can be used to calculate the performance of a search system with n detectors. It is interesting to note that the equation is independent of detector size, scan velocity, etc. used in the analysis.

Source Irradiance

The irradiance or the received energy at the aperture of the infrared system from the reentering Apollo spacecraft can be calculated as follows:

The radiation from the source, the Apollo Command Module, is considered to consist only of thermal body radiation, although there is reason to believe that the total radiation level would be in excess of this (see page 7).

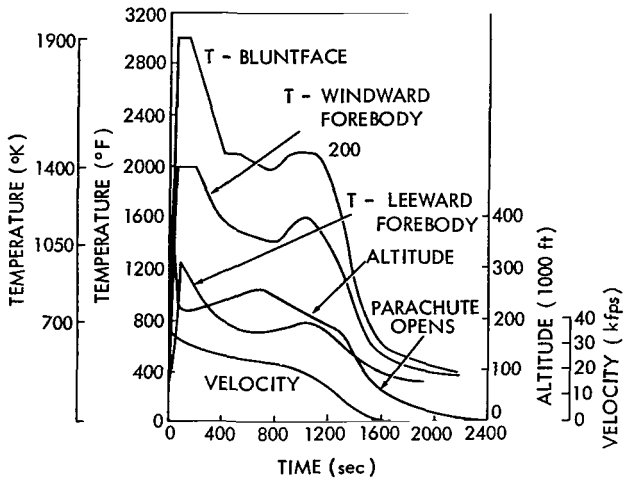

Figure 24—Surface temperature average. Typical overshoot trajectory (minimum heating conditions) Apollo—L/D 0.5 (Courtesy AVCO Corporation).

The vehicle is approaching the infrared receiver at an aspect angle whereby the blunt face of the command module is in view and the temperature distribution across the blunt face is considered to be uniform.

The mean average surface temperature level versus time for the blunt face, windward and leeward forebody of the command module are plotted in Figure 24. Also plotted are altitude and velocity versus time.*

From these curves and from the previous analysis (page 15), it is not unreasonable to calculate a radiance value based on a 1000°K target which represents a conservative figure.

There are several good reasons for considering a minimum temperature condition: one is the desire to acquire the spacecraft shortly after reentry (considered to start at 400,000 feet), another is to be able to acquire the vehicle at any aspect angle, and still another reason is the desire to maintain tracking during any skip trajectory where the heating rate is reduced.

The emissivity of the charing ablative coat on the spacecraft has been measured several times and a figure for emissivity (ϵ) of 0.75 is accepted.

The following definitions are set forth in the derivation of the equations:

A_c = area of projected blunt face of the command module (cm^2),

D_c = diameter of command module (390/cm),

T = temperature of command module (1000°K),

ϵ = emissivity of charing ablative material (0.75),

σ = Stefan-Boltzmann constant (5.673×10^{-12} watt/$cm^2 °K^{-4}$),

τ_A = transmission of the atmosphere (%),

R = range from receiver to spacecraft (kilometers),

W = radiant emittance (watts/cm^2),

J = radiant intensity (watts/steradian),

H = radiant power at receiver aperture (watts/cm^2), and

ρ = percent of total radiant power at receiver waveband response.

*Private communication from Cal Bopp, AVCO Corp., Cincinnati, 1964.

Using the mathematical statement of the Stefan-Boltzmann law, the radiant emittance can be calculated.

$$W = \sigma \epsilon T^4 \text{ watts/cm}^2 \quad . \tag{22}$$

Considering a Lambertian radiating surface,

$$J = \frac{WA_c}{\pi} \quad . \tag{23}$$

Substituting Equation 22 into Equation 23 gives

$$J = \frac{\sigma \epsilon T^4 \pi D_c^2}{4\pi}$$

$$= \frac{\sigma \epsilon T^4 D_c^2}{4} \text{ watts/steradian} \quad . \tag{24}$$

This is the total amount of radiation emanating from the source. For a temperature of 1000°K, it is interesting to note that the peak radiant intensity falls at approximately 3 microns. For a hotter target the peak intensity would fall at a shorter wavelength; however, the intensity at 3 microns would not be reduced. Conversely, for a cooler target, say 750°K, the peak radiant intensity would fall at approximately 4 microns. This relationship is shown by the series of blackbody radiation curves of Figure 25.

The irradiance at the receiver aperture may be calculated taking into account the range and atmospheric transmission:

$$H = \frac{J\tau_A}{R^2} \text{ watts/cm}^2 \quad . \tag{25}$$

Substituting Equation 24 into Equation 25 gives

$$H = \frac{\sigma \epsilon T^4 D_c^2 \tau_A}{4R^2} \text{ watts/cm}^2 \quad . \tag{26}$$

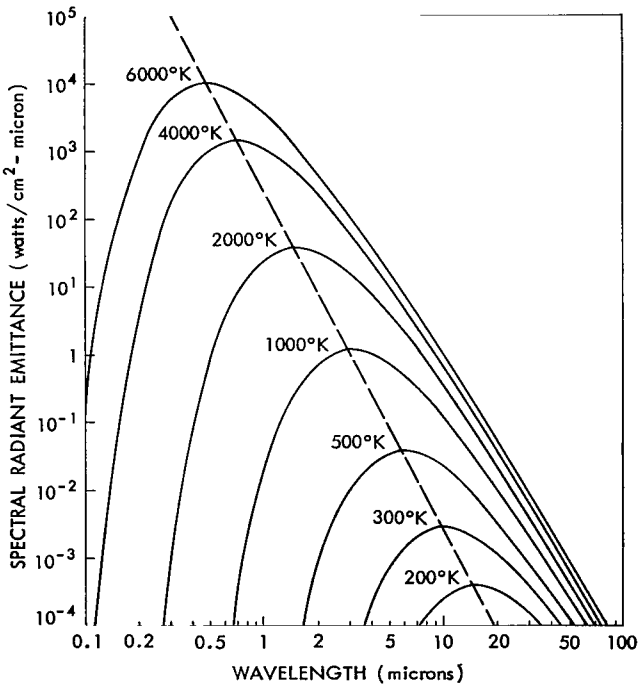

Figure 25—Spectral radiant emittance of a blackbody as a function of wavelength at various temperatures. The maximum spectral radiant emittance at a given temperature falls on the dashed curve.

This, then, is the total amount of radiant power being received at the optical collecting aperture of the infrared system.

To calculate the irradiance over the wavelength response of the infrared system, the percentage of the energy falling at the interested wavelength band is considered. The simplest method is to consult radiation tables or to use a radiation calculator such as the General Electric radiation calculator. Equation 26 is then modified by the derived percentage of radiation falling over the interested waveband:

$$H_{\lambda_1-\lambda_2} = \frac{\sigma \epsilon T^4 D_c^2 \tau_{A(\lambda_1-\lambda_2)}}{4R^2} P_{\lambda_1-\lambda_2} \quad . \tag{27}$$

Nevertheless, for an exact mathematical treatment the equations for calculating the radiant power for a waveband of interest are presented. Using Planck's law for the spectral emittance of a blackbody at a temperature, T (°K), and modified by the emissivity function, ϵ_λ,

$$W = \epsilon_\lambda \frac{C_1 \lambda^{-5}}{e^{c_2/\lambda T} - 1} \quad \text{watts/cm}^2\text{-micron} \ , \tag{28}$$

where

$$C_1 = 3.74 \times 10^4 \ \text{watts} \, \mu^4/\text{cm} \ , \text{ and}$$

$$C_2 = 1.43880 \times 10^4 \ \mu^\circ K \ .$$

Over the waveband of interest,

$$W_{\lambda_1-\lambda_2} = \epsilon_\lambda \int_{\lambda_1}^{\lambda_2} \frac{C_1 \lambda^{-5}}{e^{c_2/\lambda T} - 1} \, d\lambda \ . \tag{29}$$

The expression for receiver irradiance, $H_{\lambda_1-\lambda_2}$, can now be presented by substituting Equations 23 and 29 into Equation 25:

$$H_{\lambda_1-\lambda_2} = \frac{A_c}{\pi R^2} \int_{\lambda_1}^{\lambda_2} \frac{C_1 \lambda^{-5}}{e^{c_2/\lambda T} - 1} \epsilon_{\lambda_1} \tau_{A_\lambda} \, d\lambda \quad . \tag{30}$$

Substituting appropriate values into the equation for the irradiance, H, the radiant power received by an infrared set from the reentering Apollo spacecraft may be calculated. The simplified form

of Equation 27 is used.

$$H_{\lambda_1-\lambda_2} = \frac{\sigma \epsilon T^4 D_c^2 \tau_{A(\lambda_1-\lambda_2)}}{4R^2} P_{\lambda_1-\lambda_2} .$$

The waveband considered is the 2-2.5 micron band. $T_{A(\lambda_1-\lambda_2)}$, the atmospheric transmission for this band, was calculated to be approximately 100 percent at 40,000 feet and with a horizontal look angle; however, a more conservative figure of 70 percent is used here:

R, the slant range, is taken as 500 nautical miles = 926.5 kilometers.

$P_{\lambda_1-\lambda_2}$, the percent of total radiated energy in the 2-2.5 micron band, at 1000°K is approximately 10 percent. Therefore,

$$H_{2-3\mu} = \frac{(5.67)(0.75)(1\times10^3)^4\times10^{-12}(390)^2(0.7)}{(4)(926.5\times10^5)^2} 0.1 \text{ watt/cm}^2$$

$$= 1.32\times10^{-12} \text{ watt/cm}^2 .$$

It is interesting to compare this value for the 2-2.5 micron band to that of the 3-5 micron band, assuming the same atmospheric transmission.

For a target at a temperature of 1000°K, there is 37 percent of the total radiated energy in the 3-5 micron band. Therefore,

$$H_{3-5\mu} = (13.2\times10^{-12})(0.37) \text{ watt/cm}^2$$

$$= 4.9\times10^{-12} \text{ watt/cm}^2 .$$

To determine if this amount of radiant power at the aperture of the infrared receiver is sufficient for detection, the noise equivalent flux density (NEFD) is calculated from Equation 21. Thus,

$$\text{NEFD} = \frac{4F\sqrt{T_D S_r (n^{-1}) \Delta f}}{\pi D_o \tau_o \overline{KD^*}} .$$

An infrared system is considered which is responsive over the 3-5 micron band. Ten InSb detectors are considered, each with a 1 milliradian × 3 milliradian instantaneous field of view (FOV). A D^* value of 5×10^{10} is not uncommon for these detectors. An 8 inch collecting aperture is considered. The total FOV is the hemisphere (2π steradians). The time allowed (frame time, T_f) to scan this FOV is four seconds. The above parameters in tabular form are:

Number of InSb detectors (n) = 10,

$D^* = 5\times10^5$ cm - cps$^{1/2}$/watt,

Inst. FOV/detector (θ) = 1×10^{-3} radian (el.) and 3×10^{-3} radian (az.),

Aperture diameter (D_0) = 8 in. = 20.5 cm,

Frame time (T_f) = 4 seconds.

f/ratio (F) = 0.8,

Optical Efficiency (T_0) = 0.5, and

Signal Conversion Efficiency (K) = 0.6.

The following calculations can now be made to solve for the parameters of dwell time (T_d), search rate (S_r), and electronic bandwidth (Δf). From Equation 9,

$$S_r = \frac{AB}{T_f}, \text{ where AB for a hemisphere} = 2\pi \text{ steradians}$$

$$= \frac{2\pi}{4} = \frac{\pi}{2} \text{ steradians/sec}.$$

From Equation 20, and considering the detectors to have a 1 mr $\times$ 3 mr instantaneous FOV,

$$T_d = \frac{n\theta^2}{S_r} = \frac{2(10)\left(3\times10^{-6}\right)}{\pi}$$

$$= \frac{60\times10^{-6}}{\pi} \text{ second}.$$

InSb detectors have response time less than 1×10^{-6} second so there is no problem here of too short a dwell time. Δf, the electrical bandwidth, can be calculated from the following expression (Reference 20):

$$\Delta f = \frac{1}{3t_r},$$

where t_r is the rise time of the detector pulse output. In this case the rise time is considered equal to the dwell time, T_d, on the detector. Therefore,

$$\Delta f = \frac{1}{3T_d} = \frac{\pi}{3\left(60\times10^{-6}\right)} \text{ seconds}$$

$$= \frac{\pi\times10^6}{180}$$

$$= 17.5\times10^3 \text{ cps}.$$

Substituting the parameters into the equation for NEFD,

$$\text{NEFD} = \frac{4(0.8)\sqrt{\frac{60\times10^{-6}}{\pi}}\,(\pi/2)\,(1/10)\,\overline{17.5\times10^{3}}}{\pi(20.5)\,(0.5)\,(0.6)\,\overline{(5\times10^{10})}} \text{ watt/cm}^2$$

$$= 7.58\times10^{-13} \text{ watt/cm}^2 .$$

Comparing this value with the received power, H_λ, gives a voltage signal to noise ratio of

$$\frac{S}{N} = \frac{H_\lambda}{\text{NEFD}} = \frac{4.9\times10^{-12}}{7.58\times10^{-13}}$$

$$\frac{S}{N} \approx 6.5 .$$

This is for a target of 1000°K at 500 nautical mile range.

As in any scanning search equipment, this ratio of rms signal to rms noise can be expressed as a function of probability of detection, false alarm rate and noise bandwidth. The mathematical treatment of this relationship is quite involved and is beyond the scope of this report. The reader is referred to the work in references 16, 21, 22, 23, 24 and 25. Nevertheless, one can by a few simple calculations and the use of detection probability curves (Figure 26) determine the probability of detection for false alarm time and bandwidth versus signal to noise ratio.

Let

T_{fa} = the false alarm time (mean time between false alarms),

f = equivalent noise bandwidth = 17.5×10^3 cps,

T_f = frame time (time to scan 2π steradians) = 4 sec,

n_d = number of detector channels = 10,

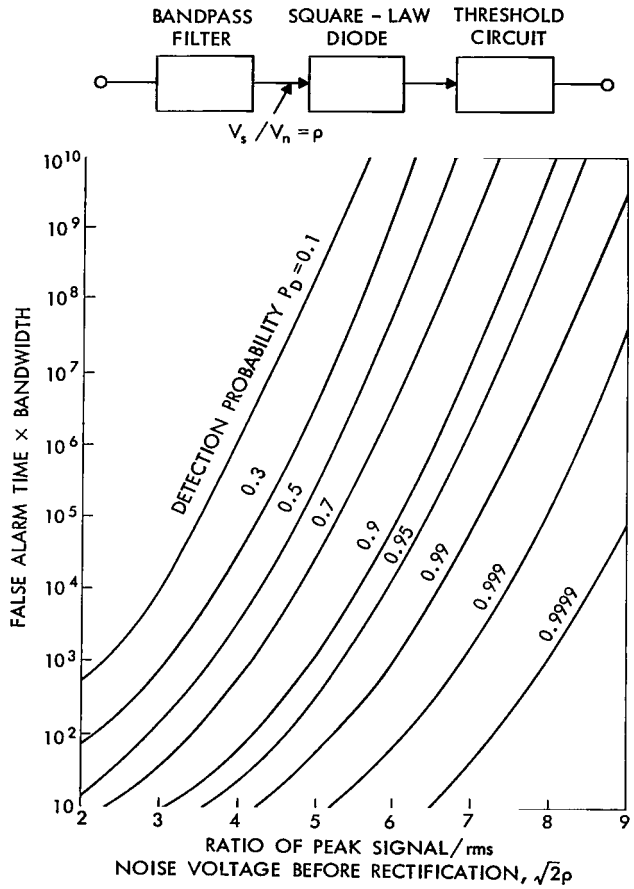

Figure 26—Signal-to-noise ratios required for specified false-alarm rates and detection probabilities (by permission from McGraw-Hill Book Company, Inc., New York [Reference 16]).

p_r = signal to noise ratio = 6.5, and

n_f = number of false alarms allowed for each scan of the hemisphere = 0.01.

Therefore,

$$T_{fa} = \frac{Tf}{n_f} = \frac{4}{0.01} = 4\times10^2 \text{ sec/false alarm}$$

then,

$$T_{fa}\,\Delta f\, n_d = (4\times10^2)\,(17.5\times10^3)\,(10)$$

$$= 7\times10^7 \text{ samples/false alarm, and}$$

$$\log_{10} T_{fa}\,\Delta f\, n_d = 7.8451 \text{ (parameter for ordinate axis of Figure 26)}.$$

The parameter for the abscissa axis of Figure 26, the peak signal to rms noise voltage, is $\sqrt{2}p_r$. Thus,

$$\sqrt{2}\,p_r = \sqrt{2}\,6.5$$

$$= 9.2\ .$$

Entering Figure 26 at 7.8451 on the ordinate axis and 9.2 on the abscissa axis gives a detection probability of 0.999.

Accuracy Requirements

One of the major functions of the infrared system is to track the reentering spacecraft. Tracking as used in this sense involves angle tracking only. Since it is not possible to predict the reentry trajectory of a lifting body, the angle tracking information will be used to determine the approximate landing point of the spacecraft. Although the tracking information accuracy is broad, relatively speaking, it nevertheless is small as far as defining the landing point area is concerned.

The prediction of this impact area is quite important if a quick recovery of the astronauts and equipment is to be assured. Prediction by means not utilizing reentry-generated radiation is complicated by the possibility of a radio blackout during reentry. Also, if damage occurred to the spacecraft antenna during reentry, no information would be available to the ground for the location of the spacecraft.

The infrared system, nevertheless, will be able to determine the landing point to within 50 to 100 nautical miles for only one system tracking. If two systems track the spacecraft at the same time, the error in determining the landing point is reduced by a factor of 10.

Calculations in support of this tracking capability have been made by Dr. Vonbun and Dr. Kalil (References 1 and 26). These calculations assume an error of the tracker of $\pm 5 \times 10^{-3}$ radian and an error in the location of the tracker of ±2 kilometers in both longitude and latitude. A zero error is assumed for the true vertical.

With allowable tracker errors on the order of ±5 milliradians, no problem is foreseen in the mechanization of the system to achieve this accuracy if the instantaneous field of view is kept small—one to two milliradians which corresponds to 206 and 412 seconds of arc, respectively. From the standpoint of lessening the effect of sky background and of increasing the system sensitivity (see page 24), the requirement for such a small field of view is a natural consequence of the infrared system design.

The positional errors placed on the location of the tracker, ±2 km (±1.08 nautical miles), require precise navigational equipment. Two approaches are open: First, an all inertial system tied in with the infrared system could be used. Inertial systems with better than the required accuracy have been built and are presently in use. Factors which weigh heavily in the design of an inertial system include the duration of the flight before positional readout is required, accuracy of ground alignment referenced to a common coordinate system, and available updating inputs during the flight such as stellar reference and doppler navigation.

A second approach in achieving the required accuracies would be a quasi-inertial system which utilizes aircraft onboard navigational equipment and other available navigational aids in conjunction with a simplified inertial system that would provide local vertical information only. Presently available navigational aids in the Western Pacific are Loran A and Loran C. Loran A at best will give a CEP of one nautical mile. Loran C capability is 1500 feet (0.25 nautical mile) (Reference 27). The coverage of the Loran A and Loran C stations, however, is not complete over the Apollo reentry area. Approval has been granted for the construction of additional OMEGA stations which when completed would give complete worldwide coverage at accuracies comparable to Loran C. Positional heading information can be obtained from an automatic readout gyro flux-gate compass which will provide a four milliradian accuracy capability.

The choice of either approach, inertial or quasi-inertial, would of course have to weigh several factors. A few of the obvious considerations are cost, accuracy, and reliability.

CONCEPTUAL CONFIGURATION

Many scanning and optical configurations that could search the hemisphere, each with their own advantages and disadvantages, are possible. Two configurations worthy of further consideration are presented herein.

In arriving at these configurations, certain ground rules were set forth considering the mission requirements. First, the need to acquire the spacecraft quickly and to maintain track even during a skip period requires a detector responsive to the cooler skip period temperatures of the spacecraft. Second, the requirement that the infrared system perform its mission at maximum range under daylight conditions dictates that it be responsive at wavelengths where background radiation is at a minimum and that each detector have a small instantaneous field of view. Third, the need to scan the hemisphere rapidly requires many detectors, each with a slow response time, or few detectors, each with fast response time.

Indium antimonide (InSb) was chosen as the detector because of its fast response and high detectivity at the wavelength region of the spacecraft thermal body radiation and because over this region, background radiation is at a minimum.

The need to acquire the spacecraft quickly would indicate that the most desirable wavelength band is the 8-13 micron window (the blackbody radiation from a 25°C object peaks at 10 microns). A system responsive at this wavelength in effect would permit "cold body" acquisition of the Apollo spacecraft even prior to reentry. Unfortunately, the atmospheric radiation also is slightly stronger at these wavelengths (page 19) than over the 3 to 5 micron band and detectors sensitive at these wavelengths require liquid helium cooling.

As mentioned before (page 6), a predominant dip in the sky background radiation occurs conveniently across the 3 to 5 micron band (Figure 7). The temperatures which correspond to the peak blackbody radiation falling at these wavelengths are 675° and 300°C, respectively. The time history versus heat rate input and surface heating for a nominal reentry trajectory shows that a surface temperature of 860°C will be reached in less than 10 seconds after reentry (Reference 28). At this time, the spacecraft will be at 350,000 foot altitude. Detectors responsive over the 3 to 5 micron band require liquid nitrogen cooling, but this is not considered a drawback because complex scanning systems utilizing liquid nitrogen detector cooling are commonly in operational use by the military services all over the world. These detectors have fast time constants, <1 microsecond, and only a few are required to scan the hemisphere in the allowed time.

Systems containing many detector elements can be fabricated by utilizing film deposition techniques. Films commonly employed such as PbS are responsive in the 2 to 2.5 micron region. Although the PbS detector systems have a lower noise equivalent power than the InSb systems commonly employed over the 3 to 5 micron region, they are subject to a higher environmental background radiation, variation, and false target inputs (page 17). PbS detectors have slow response times and therefore many detectors would be required to search out the hemisphere in the frame time allowed. Associated with the utilization of many detector elements is the electronic complexity of the signal amplification, commutation, and data handling. It is estimated that more than 100 PbS detectors would be required, each with its own preamplifier. However, work has been done to reduce the complexity of "many-element" systems by using molecular electronics (Reference 29). A further disadvantage of these systems is that wide field of view, short focal length optics are required. The two conceptual systems presented in Figures 27 and 28 operate over the 3 to 5 micron band utilizing ten InSb detectors, each detector having a 1 mr elevation by

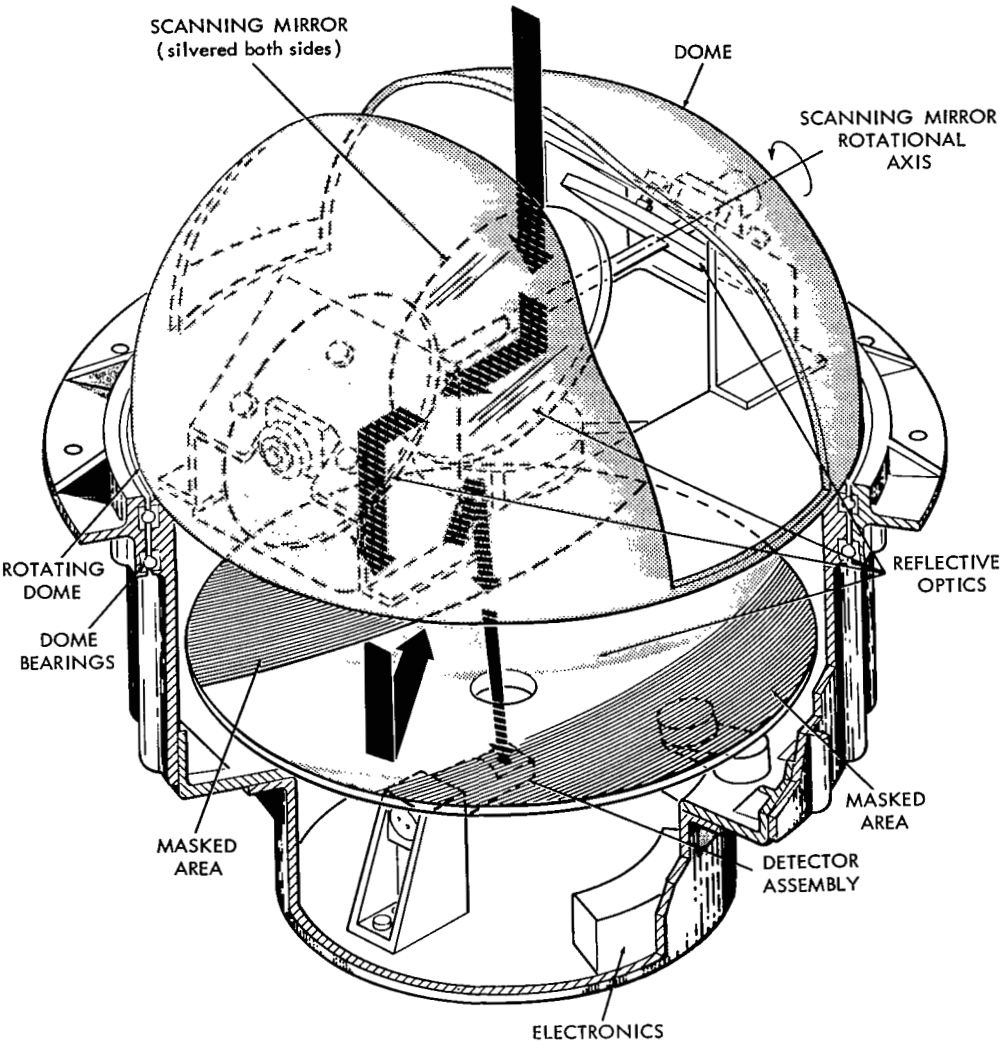

Figure 27—GSFC infrared hemispherical scanner, conceptual design.

a 3 mr azimuth instantaneous field of view. The ten elements are arranged in a linear array parallel to the horizontal plane of the scanner.

The more apparent advantage of the configuration in Figure 27 is the low profile of the turret, generating little disturbance to the air flow external of the aircraft skin. Although there are four reflective surfaces that would attenuate an incoming ray, these surfaces can be made 95 percent reflective and the total efficiency of the optical system would be on the order of 81.5 percent. The disadvantage of the optical configuration perhaps is the requirement for a large primary mirror on the order of 24 inches in diameter; however, large portions of this mirror can be masked off to reduce scattered light effects. Note that there is no obscuration of the incoming rays by the secondary mirror. The projected image of the detector array field of view would rotate from horizontal at the horizon to vertical at zenith as the system scanned from horizon to horizon. This

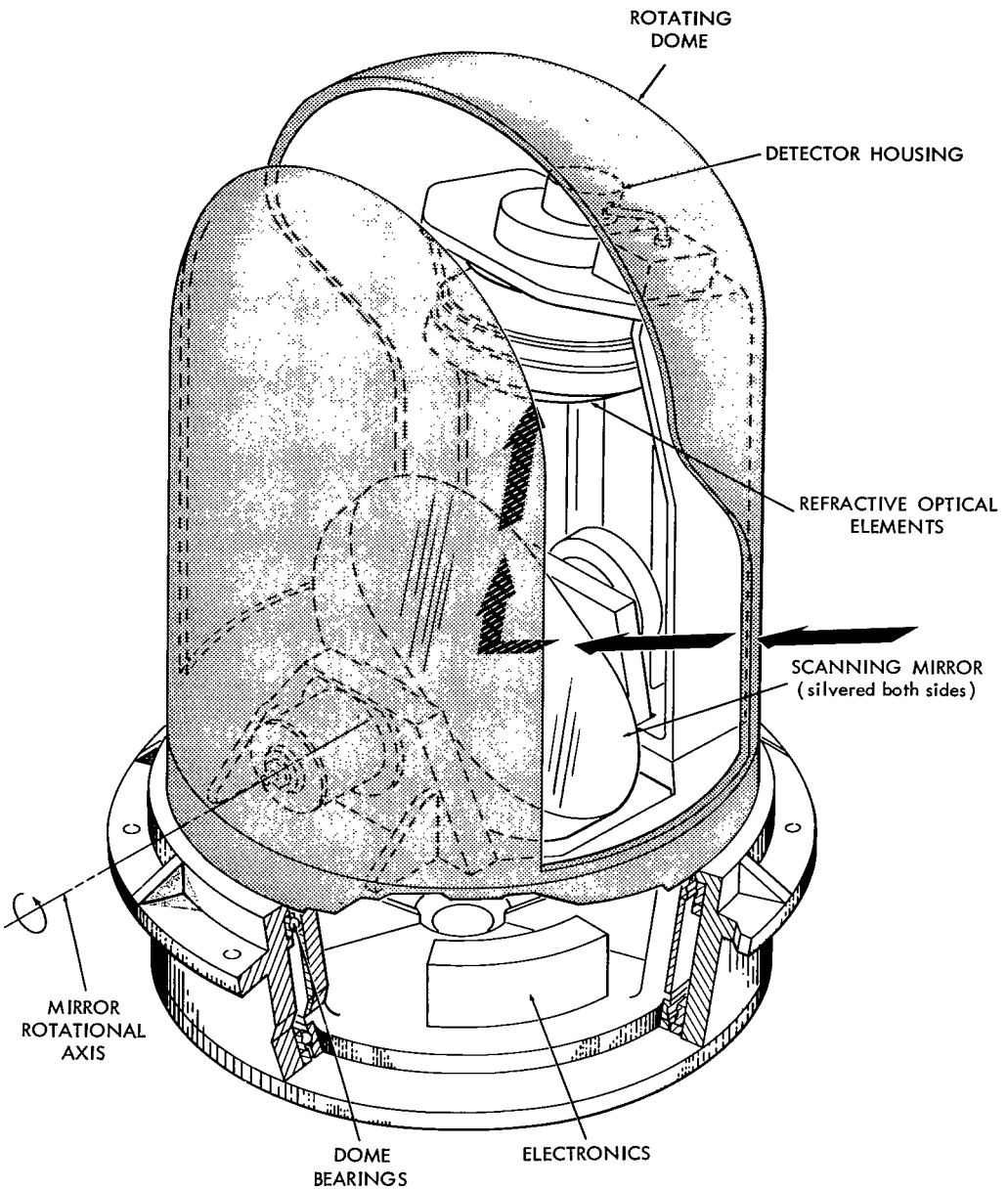

Figure 28—Infrared hemispherical scanner utilizing the refractive optical elements from the Aerojet W48 scanner.

would not permit overlap coverage at near zenith angles, which is considered a desirable feature.

Another advantage of this system is that access could be gained to the detector-electronic area for servicing inside the aircraft. Also, no scan dead time is lost as the mirror rotates and imaging is achieved for 100 percent of a mirror rotation cycle.

The advantage of the configuration in Figure 28 is the compactness of the unit (however, the turret would project further into the slip stream outside the aircraft skin). Also, there is very little rotation of the image plane projected back into the hemisphere as the system scans through zenith. Therefore, overlap coverage would be obtained with this system. Refractive focusing optical elements are considered in conjunction with the scanning mirror (polished on both sides) giving an estimated optical efficiency of 60 percent. If the refractive elements were replaced with Cassegrainian optics, a total of three reflective surfaces would then attenuate the signal and the optical efficiency would be increased to 85.5 percent. Further disadvantages of the system are the inability for service access internal to the aircraft and the scan dead time, 25 percent of each mirror rotation.

In both systems the opening in the turret dome is narrower at the top than on the sides. This is because when viewing the spacecraft at high zenith angles (closer range) the intensity is greater and the aperture opening can be reduced to lessen the required dynamic range of the detector and signal processing electronics.

To provide an environmental seal for the dome and to maintain the aerodynamic shape of the turret, a window encloses the turret opening. This window can be made up of large flat pieces of infrared transmitting material, thereby circumventing the problems of curved dome surfaces and associated optical effects.

The above comments on both systems are superficial and of course, as with any complicated electro-optical-mechanical system, a more detailed analysis would have to be performed before a decision could be made as to what system represented the best compromise. The author is also aware that there are other scanning configurations in addition to those presented herein that would merit consideration.

APPLICABLE STATE OF THE ART

General

Many infrared systems have been built and have successfully met design objectives. These systems range from the aerial and spacecraft search and reconnaissance type to the electronic component checker found on manufacturing production lines.

Familiar Infrared Systems

Some of the more familiar devices are the highly successful Sidewinder missile which is guided to the target by virtue of its infrared seeker; the sniperscope developed during World War II for nighttime viewing of enemy troop operations; the circuit tester used to determine "hot" circuit components as a means of bettering component or system reliability; and the Tiros-Nimbus satellite radiometers used to obtain cloud temperatures and pictures over the dark side of the earth.

Applied Technology

Great advances have been made in the field of applied infrared technology and there are a number of wide field of view search systems, some with track-while-scan capability, that demonstrate the design feasibility of a hemispherical search, lock-on, and track system at the sensitivity and search rate discussed in this report.

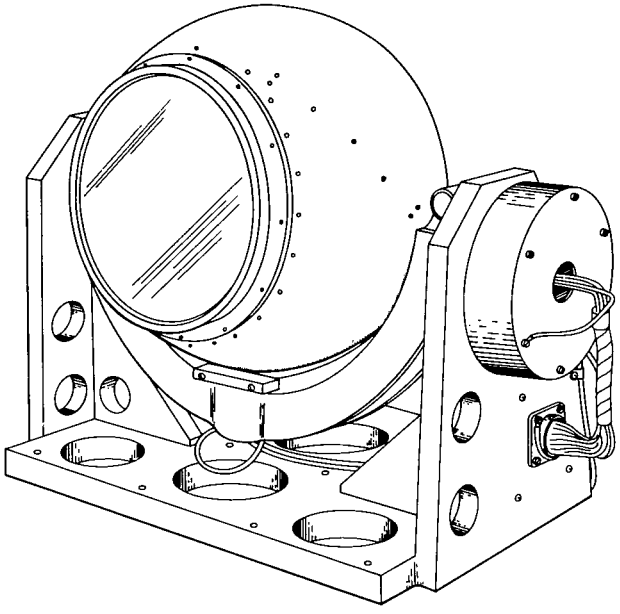

Figure 29—Aerojet Model W48 infrared search system.

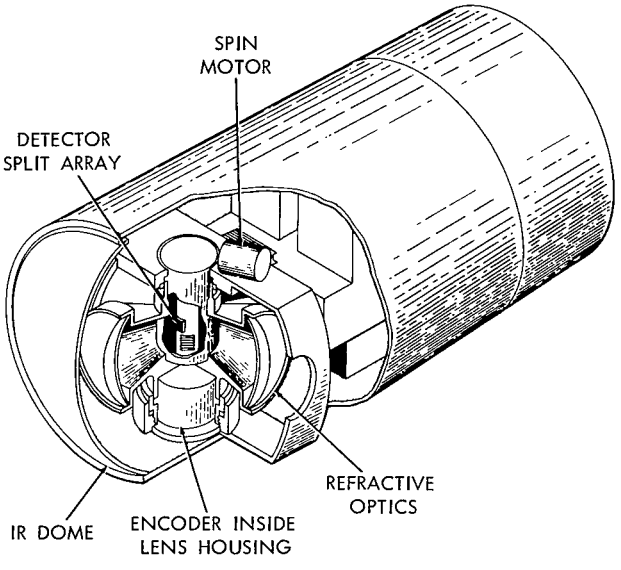

Figure 30—AVCO drum scanner.

It is difficult for one not directly associated with the field of infrared technology to appreciate the scope of the advances that have been made and to be knowledgeable of the many varied systems that have been successfully built. This general lack of knowledge of the state of the art in infrared technology is with good reason understandable. Much of the data, techniques, and systems which demonstrate the state of the art are classified for military reasons.

Two systems are presented (Figures 29 and 30) which have a wide field of view coverage, small instantaneous fields of view, fast response, and high detectivities. Suffice to say that there are other systems and there are more advanced operational versions of these systems which are classified. The reader is referred to the following documents for further information: Research and Development of Infrared Track-While-Scan Technique, AD337-583, Secret; AN/ALR-23 Infrared Countermeasure Receiver Set, Secret, AVCO Electronics Division, Cincinnati, Ohio; Development and Testing of the Airborne Infrared Early Warning System (AIREW), NAVWEPS Report 7887, NOTS TP2877, Secret; Infrared Discrimination Investigation, AD 345-671, Secret.

Figure 31 shows the field of view obtainable with the AVCO Drum Scanner. It does not take much imagination to picture the drum scanner, for example, mounted on a turntable such that the 90° coverage is now in the vertical direction with the turntable rotating in azimuth providing 360° coverage, thereby covering the hemisphere. With this configuration (Figure 32), the total hemisphere would be scanned in approximately

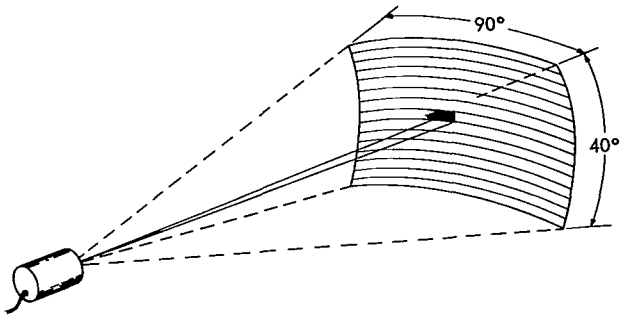

Figure 31—AVCO drum scanner (Search/Track System) scan field. Total search field covered three times per second is 90° wide x 40° high.

three seconds with overlap coverage at high elevation angles. The disadvantage in utilizing a drum scanner of the type described above is that small collecting aperture optics (approximately 3-1/2 inches in diameter) are used, thereby limiting the range capability.

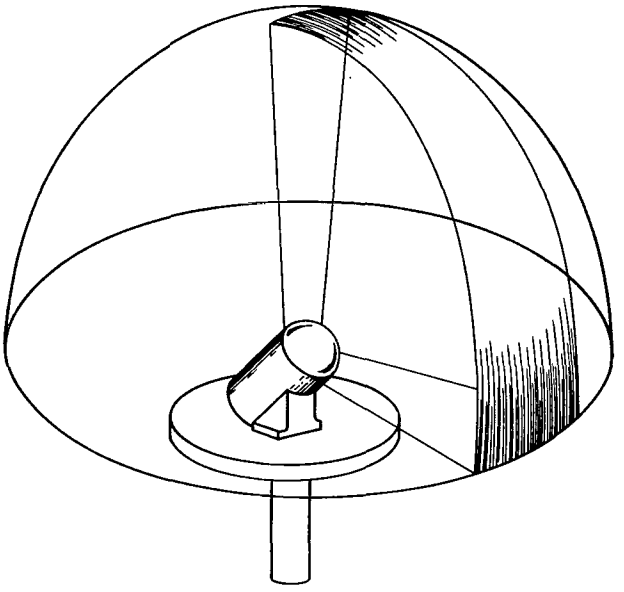

Figure 32—Drum scanner mounting for hemispherical coverage. Hemisphere is covered in approximately 3 seconds.

ACKNOWLEDGMENTS

The author wishes to acknowledge the contribution of Dick Higby of the Westinghouse Electric Corporation in the theoretical approach in defining the spacecraft surface temperature boundary conditions, that of Fred Pitts of Booz-Allen Applied Research Incorporated in his active support during many phases of the project, especially in the preparation of the system specifications, and that of other Booz-Allen personnel in their investigation of aircraft navigational aids.

He is also thankful to Ken Nagler of the U. S. Weather Bureau, who personally undertook a study on the problem of defining the cloud cover over the Apollo reentry area; to the personnel at the Institute of Science and Technology, University of Michigan, and in particular to Roy Nichols, who was primarily responsible for generating the thermal-spectral profile of the reentering Apollo spacecraft (Appendix B); to Brian Erb of the Thermal Structures Branch, Manned Space Flight Center, for making available to the University of Michigan the data necessary to accomplish the thermal-spectral profile analysis; to Bill Page of Ames Research Center for the stimulating discussions and data provided on reentry body radiation and measurement techniques; to John A. Jamieson of the Aerojet-General Corporation and Cal Bopp of AVCO for their assistance in the project; and to Lou Meuser of Wright Patterson Air Force Base for his support and cooperation in providing data on IR system specifications.

(Manuscript received December 10, 1965)

REFERENCES

1. Vonbun, F. O., "Apollo Re-entry Infrared Support," GSFC Document X-513-65-4, December 1964.

2. Lehnert, R., and Rosenbaum, B., "Plasma Effects on Apollo Re-entry Communication," NASA TN D-2732, March 1965.

3. Craig, R. A., and Davey, W. C., "Thermal Radiation from Ablation Products Injected into a Hypersonic Shock Layer," NASA TN D-1978, September 1963.

4. Page, W. A., and Arnold, J. O., "Shock-Layer Radiation of Blunt Bodies at Re-entry Velocities," NASA TR R-193, April 1964.

5. Page, W. A., "Shock-Layer Radiation of Blunt Bodies Traveling at Lunar Return Entry Velocities," 31st Annual Meeting, Institute of the Aerospace Sciences, January 21-23, 1963, Paper No. 63-41, New York: 1963.

6. "Infrared Sensor for Apollo Re-entry Vehicles," Final Report, Westinghouse Aerospace Division Contract NAS5-9703, Baltimore: 1964.

7. Little, B. H., Jr., "Aerodynamic Heating for Lunar Re-entry Vehicles," in: *Advances in the Astronautical Sciences*, Vol. 2, ed. by H. Jacobs, North Hollywood, California: Western Periodicals, 1963, pp. 767-797.

8. Lees, L., "Recovery Dynamics-Heat Transfer at Hypersonic Speeds in a Planetary Atmosphere," in: *Space Technology*, ed. by H. S. Seifert, New York: John Wiley, 1959, pp. 1201-1220.

9. Kivel, B., "Radiation from Hot Air and Its Effect on Stagnation-Point Heating," *J. Aerospace Sci.* 28:96-102, February 1961.

10. Meyerott, R. E., Sokoloff, J., and Nicholls, R. W., "Absorption Coefficients of Air," "Bedford, Mass.: Geophysics Research Directorate, Air Force Cambridge Research Center, July 1960.

11. Kruse, P. W., McGlauchlin, L. D., and McQuistan, R. B., "Elements of Infrared Techology, Generation, Transmission and Detection," New York: John Wiley, 1962.

12. Altshuler, T. L., "Infrared Transmission and Background Radiation by Clear Atmospheres," Philadelphia: General Electric Co., Space Science Lab., December 1, 1961.

13. Murcray, D. G., Murcray, F. H., and Williams, W. J., "Variation of the Infra-red Solar Spectrum between 2800 and 5100 cm with Altitude," *J. Opt. Soc. Amer.* 54(1):23-27, January 1964.

14. Bennet, H. E., Bennett, J. M., and Nagel, M. R., "Distribution of Infrared Radiance over a Clear Sky," *J. Opt. Soc. Amer.* 50(2):100-106, February 1960.

15. Bell, E. E., Eisner, L., Young, J., and Oetjen, R. A., "Spectral Radiance of Sky and Terrain at Wavelengths between 1 and 20 Microns. II. Sky Measurements," *J. Opt. Soc. Amer.* 50(12): 1313-1320, December 1960.

16. Jamieson, J. A., McSee, R. H., Ploss, G. N., Grube, R. H., and Richards, R. G., "Infrared Physics and Engineering," New York: McGraw-Hill, 1963.

17. Walker, R. G., and D'Agati, A., "Infrared Stellar Irradiance," *Applied Opt.* 3(11):1289-1292, November 1964.

18. Hall, F. F., Jr., "Results of an Infrared Stellar Mapping Program," in: *Les Spectres Infrarouges des Astes, Communications Presentées a Douxiéme Colloque International d'Astrophysique a Liège, 24-26 Juin 1963,* Liège: Institut d'Astrophysique, 1964.

19. Jones, R. C., "Phenomenological Description of the Response Detecting Ability of Radiation Detectors," *Proc. IRE,* 47(9):1495-1502, September 1959.

20. Moskowitz, S., and Racker, J., "Pulse Techniques," New York: Prentice Hall, 1951.

21. Peterson, W. W., Birdsall, T. G., and Fox, W. C., "The Theory of Signal Detectability," *IRE Trans. on Inform. Theory,* PGIT-4:171-212, September 1954.

22. Middleton, D., and Van Meter, D., "Detection and Extraction of Signals in Noise from the Point of View of Statistical Decision Theory I," *J. Soc. Ind. Appl. Math.* 3(4):192-253, December 1955.

23. Middleton, D., and Van Meter, D., "Detection and Extraction of Signals in Noise from the Point of View of Statistical Decision Theory II," *J. Soc. Ind. Appl. Math.* 4(2):86-119, June 1956.

24. Marcum, J. I., "A Statistical Theory of Target Detection by Pulsed Radar: Mathematical Appendix," California: Rand Research Corp., RM-753, July 1, 1948.

25. Rice, S. O., "Mathematical Analysis of Random Noise," ed. by N. Wax, New York: Dover Publications, 1954, pp. 133-194.

26. Kalil, F., "Infrared Acquisition and Tracking System - Preliminary Mission Specifications," Technical Brief, Systems Analysis Office, GSFC December 9, 1964.

27. Richard, H. L., "Navigational Capabilities of JC-135 Equipment Over the Projected Apollo Re-Entry Areas," Memorandum dated December 3, 1964, Optical Systems Branch, Advanced Development Division, GSFC.

28. "Heat Rate for an Overshoot and Undershoot Re-entry Trajectory," Thermo Structures Branch, Manned Space Flight Center, 1964.

29. "Molecular Search-Track Infrared System," Final Report, Westinghouse Aerospace Division Contract AF 339616)8449, Baltimore: 1964.

Appendix A

The Effect of Clouds Above 35,000 Feet on Infrared Spacecraft Tracking Over the Western Pacific Ocean

Kenneth M. Nagler
Spaceflight Meteorology Group
National Weather Satellite Center
U. S. Weather Bureau
Washington, D. C.

November 20, 1964

Introduction

In evaluating the possible use of an airborne Infrared Reentry Acquisition Seeker (IRAS) at an altitude of about 35,000 feet, it is necessary to know something about the clouds which exist above that level in the region in which the spacecraft reentry is planned. For the Apollo mission, the reentry according to present plans (Reference A1) would most likely occur between the equator and 35N and between 140E and 170W for a landing in the proposed northern hemisphere landing area just east of the Hawaiian Islands. For the proposed southern hemisphere landing area east of American Samoa, the probable limits of the reentry area would be from the equator to 35S and between 130E and 180 degrees. The reentry probability would, of course, be much higher for certain small portions of these areas.

An attempt has been made to assess the effect of clouds above 35,000 feet in this region. In practically no area of the world is there sufficient information on which an accurate evaluation of the effect of clouds above such a level could be based. In the region of concern there is very little information for such an evaluation. Nevertheless, with considerable subjectivity it is possible to come to some general conclusions of the probable effect of clouds above 35,000 feet on an operation using the IRAS to track a reentering Apollo spacecraft.

Figures A1 through A4 show relative zones of cloud cover above 35,000 feet for the months of February, May, August, and November. The significance of the zones and the sources of information are discussed below.

Discussion of Figures A1 - A4

The boundaries of the zones and the significance of the zones must be considered as very rough, resulting from limited and questionable data and subjective judgment.

In Zone A, the best for operation of the IRAS, there is a low frequency of high clouds, such that 90 percent of the time, or more, clouds should not interfere substantially for high view angles (within about 45 degrees of the zenith). As the viewing angle approaches the horizon, naturally, the chances for successful tracking are diminished, but even for low viewing angles the chances are fairly good in this zone.

In Zone B, there should be sufficiently clear skies above 35,000 feet for high-angle viewing between about 50 and 90 percent of the time, with a lesser chance for lower viewing angles. Extratropical disturbances will cause intermittent cloudiness on the poleward portions of this zone, while closer to the equator various tropical weather disturbances will contribute to the high cloudiness.

In Zone C, good viewing conditions for even high angles would occur less than half of the time, and chances for success at low angles would be very small.

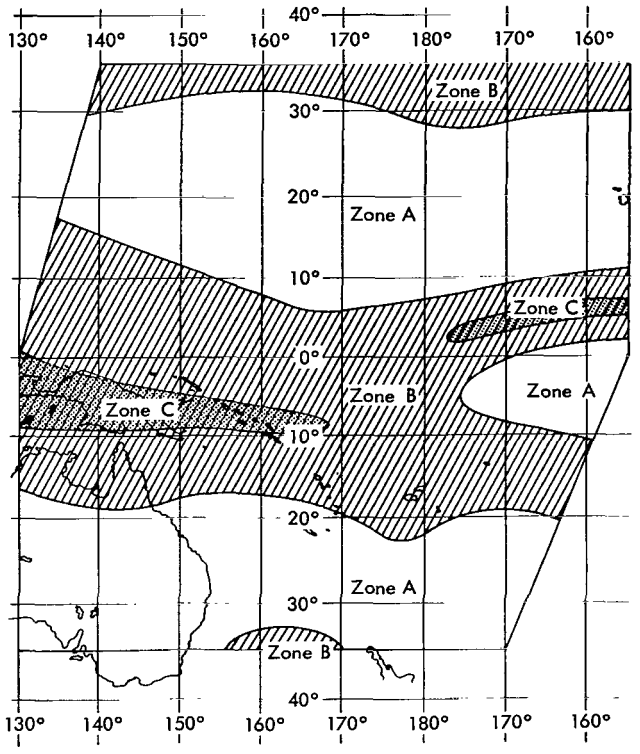

Figure A1—Zones indicating the relative chances of success of an IRAS mission at 35,000 feet, February (see text for explanation).

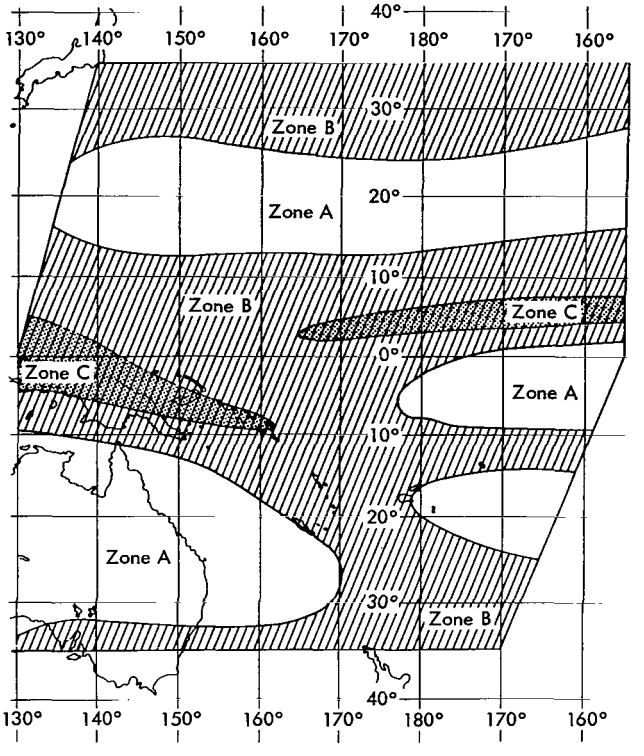

Figure A2—Zones indicating the relative chances of success of an IRAS mission at 35,000 feet, May (see text for explanation).

As to the nature of the clouds likely to occur above 35,000 feet, cirrus (ice-crystal) clouds would be by far the dominant type, but at times there would be some towering cumulus or alto-cumulus composed of water droplets.

The cirrus clouds in the area are of a number of varieties, ranging from widely scattered wispy patches of cirrus uncinus (H-1 in the international code) to thick cirrostratus overcast (H-7 in the international code). In the equatorial convergence area and in the various disturbances which are intermittent much of the cirrus is of the spissatus variety, originating from the upper portions of cumulonimbus clouds but moving away from and persisting much longer than the parent clouds. These cirrus can vary greatly in their thickness, uniformity, and areal extent.

In the higher latitudes in the area of concern, particularly in the winter season, some of the cirrus—again varying considerably—is that associated with the jet stream (the high speed core of the upper westerly winds). Particularly in the tropics, the cumuliform clouds extend well above 35,000 feet. In disturbed areas such clouds would be very common, with a number of individual storms or lines or areas of storms within sight of a high flying aircraft.

Sources of Information

1. Aircraft observations. The most direct of the information sources is the summary of cloud observations above 35,000 feet in the area of concern prepared by the National Weather Records

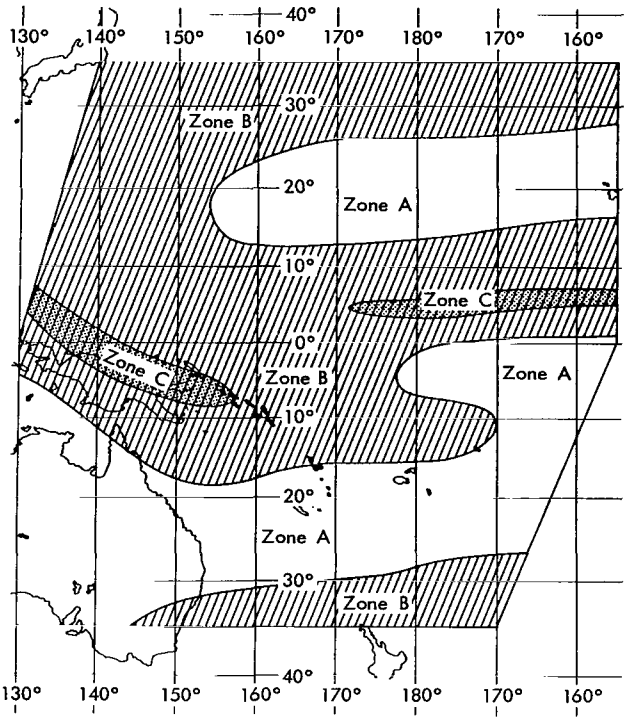

Figure A3—Zones indicating the relative chances of success of an IRAS mission at 35,000 feet, August (see text for explanation).

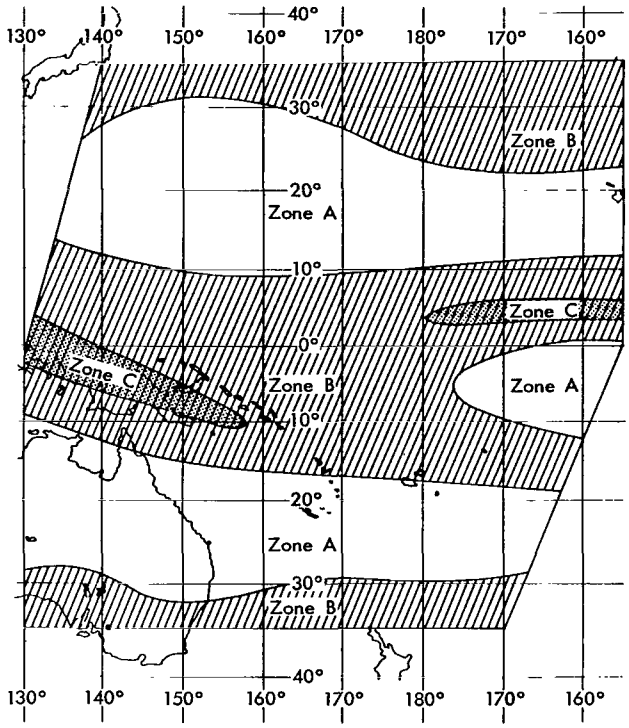

Figure A4—Zones indicating the relative chances of success of an IRAS mission at 35,000 feet, November (see text for explanation).

Center, Asheville, North Carolina, specifically for this study. Based on high-level aircraft weather observations in the period 1959 through 1963, frequencies of layer clouds above 35,000 feet were compiled in three categories: One to five-tenths of the sky covered, more than five-tenths of the sky covered, and layer clouds reported, but amount not stated. The frequency of cumulus clouds reported above 35,000 feet was also compiled, although the fraction of the sky covered was not considered since such information was not generally available in the reports. The observations were summed for each 5-degree "square" of latitude and longitude.

These data have several shortcomings. The most significant is that observations are available for only a small portion of the area of concern, namely along the air routes between Honolulu and Japan, Honolulu and the Philippines, and between Honolulu and New Zealand and eastern Australia. No reports were available for most of the area.

Also, there are not enough observations to give valid, long-range statistics. Finally, there may be biases in aircraft observations—biases whose effects are hard to judge. Pilots making routine inflight weather observations may sometimes ignore clouds well above them or may not report thin cirrus clouds, thus leading to an underestimate of the frequency of high-level clouds.

On the other hand, the failure to report thin cirrus clouds may, in fact, yield statistics more applicable to the IRAS evaluation. The thin clouds not reported might well be sufficiently transparent in the infrared to permit spacecraft tracking—at least for high viewing angles.

2. Infrared observations from TIROS IV. Several meteorological satellites have yielded infrared radiation measurements which can be used to approximate the temperature of the radiating cloud "surface" and hence the altitude of the cloud tops, as discussed, for example, by Bandeen, Halev, and Strange (Reference A2). The information already processed is generally in the form of averages for various time periods and averages over fairly large areas. Either form of averaging makes the results difficult to interpret, since the average value may be representative of a cloud-top height generally present over the area and period involved, or it may be an intermediate value between higher and lower cloud heights which were present in the area or time period over which the average was made.

One set of daily infrared radiation values averaged for relatively small areas (2-1/2 degrees of latitude on a side) were available from TIROS IV from a study made by the Planetary Meteorology Branch, Meteorological Satellite Laboratory, National Weather Satellite Center. The frequencies of radiation values equal to or less than 0.20 ly min^{-1}, 0.23 ly min^{-1}, and 0.26 ly min^{-1} were abstracted for each of these areas for February and May of 1962 and grouped (for convenience) in 5-degree squares.

The exact significance of the selected radiation values is difficult to assess in terms of cloud height (1) because of calibration difficulties in relating the values to specific black-body temperatures, (2) because the radiation, particularly in the case of cirrus clouds, is not just from the upper surface but comes in part from within or even below the cloud, depending on its density, and (3) because the level in the atmosphere associated with a specific temperature (and hence radiation value) varies with location and with time.

For most of the area under consideration (except for the higher latitudes) the height equivalents were estimated very roughly as follows:

0.20 ly min^{-1}	38,500 feet
0.23	34,500
0.26	30,000

The frequencies of radiation values of 0.26 ly min^{-1} or less (Figures A5 and A6) were considered of greatest significance in this study even though the estimated black-body temperature represented would indicate a cloud height of about 30,000 feet rather than 35,000 feet. Comparison with other data gave the impression of a better fit of the 0.26 ly min^{-1} values, probably because there is an averaging over an area and perhaps because of calibration errors in assessing the raw data.

These frequencies showed the abundance of high cloudiness in the convergence zone and the sparsity of high clouds in the subtropics. They represent only partial coverage for one February and one May, however, so may deviate substantially from valid long-period data; therefore, they were used as guidance material only.

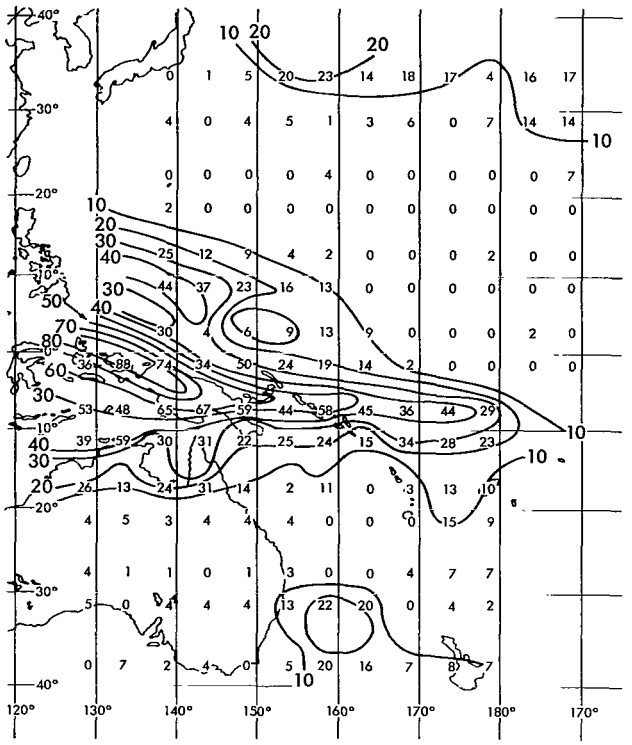

Figure A5—Frequency of infrared radiation values of 0.26 ly/min or less as estimated from TIROS IV, February 1962.

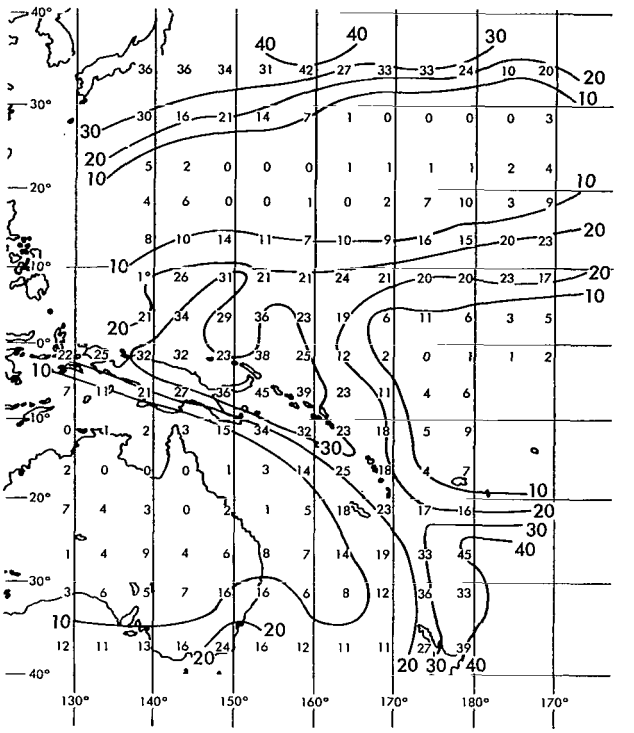

Figure A6—Frequency of infrared radiation values of 0.26 ly/min or less as estimated from TIROS IV, May 1962.

3. Surface observations. From land stations in the area there are records of cloud observations which could be used to get statistics on high clouds of various types. Also, records of weather observations from ships could be used to get frequencies of various cloud types and amounts for various subdivisions of the area of concern.

There are several obvious shortcomings in the use of surface weather observations to assess cloudiness above 35,000 feet, however. For one thing, estimates of the heights of high clouds are not normally given, and, even when available, are not very reliable. Also, whenever there are abundant low or middle clouds, observing the high clouds is either impossible or unreliable.

Accordingly, in this initial survey of the distribution and effects of clouds over 35,000 feet in height, surface observations have been used only where available in convenient summaries and only for areas where lower clouds are not very abundant.

Specifically, (from Reference A3) cloud data for Australia were used in the evaluation; and from U. S. Navy (Reference A4) available analyses of the frequency of relatively clear areas ($\leq$ two-tenths total sky cover) were considered in drawing the maps of clouds above 35,000 feet, as were analyses of the frequency of precipitation—as an indication of areas of substantial cloudiness.

4. TIROS cloud pictures. Average cloud cover charts have been prepared from TIROS nephanalyses by several investigators, notably Clapp (Reference A5). The TIROS cloud pictures and the resulting analyses are not suited for quantitative cloud height determination, but the patterns of cloud cover are useful in judging the locations of the clearer or stormier areas, and hence the areas of probable minimum and maximum frequencies of high clouds.

5. Other sources of information. There are a great many articles in the meteorological literature which bear on the general subject of high clouds or which give some specific information for pertinent parts of the world. These contributed to a general impression of what to expect in the reentry area but did not give specific information. Articles of a general nature include those by Palmer, Nicholson, and Shimaura (Reference A6) and Stone (Reference A7).

As an example, there are a number of studies dealing with the high clouds associated with the jet stream, such as those of Schaefer (Reference A8), Conover (Reference A9), Riehl (Reference A10), and Kadlec (Reference A11). Most such studies have been made over North America but can be used in evaluating cloudiness over the higher latitudes of the possible reentry area, where the jet stream is common and well developed in the winter half of the year.

Limited but specific information on high tropical cloudiness is given by Littlejohns (Reference A12) and Ryan (Reference A13).

Conclusion

Although there are many uncertainties, it appears that chances for acquisition and tracking of the incoming spacecraft by means of the IRAS would be good for most of the area of concern. At or above an altitude of 35,000 feet in both hemispheres there is a zone where cloud cover is sufficiently good most of the time even for low viewing angles. There is also a zone—primarily in the equatorial region where high cloudiness is very common, so that the IRAS would not have a good chance of working well. Even here, however, if there is a capability of moving to a different location, say fifty miles or so distant from the optimum site for a particular reentry, the chances are fair for at least partial coverage.

Problems and Recommendations

This study has been of a preliminary nature, but there is not adequate information available to give accurately the probabilities for successful use of the IRAS over the Western Pacific area even if a more sophisticated study were attempted.

Some additional information could be developed, however, if the time and effort are warranted:

1. Further use of TIROS and possibly NIMBUS infrared radiation data could be made. For example, with some programming and considerable computer time, the frequency distribution of the radiation values for the smallest area observed by the radiometer (about 60 km on a side for a view straight down) could be obtained.

2. Aircraft weather observations not on file at National Weather Records Center, Asheville, North Carolina, could probably be obtained from other sources, for example, from airlines or from other countries with frequent flights in the Western Pacific.

3. Further information could be obtained from summaries of surface weather observations which could cast some light on the upper cloud statistics, but which would still have the shortcomings mentioned earlier.

4. Perhaps some arrangement could be made to obtain more detailed in-flight reports tailored to the IRAS problem, by direct contact with one or more of the airlines with routes in the area of concern.

5. The ideal (and most expensive) approach is the scheduling of special flights to add to the climatology of clouds above 35,000 feet, but, mainly, to measure the effects of cirrus on simulated operations using some prototype IRAS equipment.

References

A1. Vonbun, F. O., "Re-Entry Tracking for Apollo" Goddard Space Flight Center, GSFC Document X-513-64-85, March 6, 1964.

A2. Bandeen, W. R., Halev, M., and Strange, I., "A Radiation Climatology in the Visible and Infrared from the TIROS Meteorological Satellites," prepared by GSFC for International Radiation Symposium, International Association of Meteorology and Atmospheric Physics (IUGG) Leningrad, August 1964.

A3. Rofe, B., "Geophysical and Meteorological Data of Woomera Ranges," Commonwealth of Australia, Weapons Research Establishment.

A4. "Marine Climatic Atlas of the World," Volumes II, III and V. North Pacific Ocean NAVAER 50-1C-529, 1956; Indian Ocean NAVAER 50-1C-530; 1957; and South Pacific Ocean NAVAER 50-1C-532, U. S. Navy, 1959.

A5. Clapp, P. F., "Global Cloud Cover for Seasons Using TIROS Nephanalyses," *Month. Weath. Rev.* 92(11):495-507, November 1964.

A6. Palmer, C. E., Nicholson, J. R., and Shimaura, R. M., "An Indirect Aerology of the Tropical Pacific," Wahiawa, Hawaii: University of California Institute of Geophysics, Oahu Research Center, June 1956.

A7. Stone, R. G., "A Compendium on Cirrus and Cirrus Forecasting," Air Weather Service Technical Report TR 105-130, Military Air Transport Service, March 1957.

A8. Schaefer, V. J., "The Use of Clouds for Locating the Jet Stream," *Aeroplane*, 85(2206):599-602, October 30, 1953.

A9. Conover, J. H., "Cloud Patterns and Related Air Motions Derived by Photography," Milton, Mass.: Blue Hill Meteorological Observatory, 1959.

A10. Riehl, H., "Jet Streams of the Atmosphere. Technical Paper No. 32. Department of Atmospheric Science," Fort Collins, Colo., Colorado State University, May 1962.

A11. Kadlec, P. W., "A Study of Flight Conditions Associated with Jet Stream Cirrus, Atmospheric Temperature Change, and Wind Shear Turbulence," Miami, Fla., Eastern Air Lines Meteorological Dept., June 1964.

A12. Littlejohns, L. W., "High Cloud Structure in Equatorial Southeast Asia," *Meteor. Magazine* 87(1032):172-179, June 1958.

A13. Ryan, P., "Height of Cirrus Cloud Tops in Tropics," *Australian Meteor. Magazine* 25:76-77, June 1959.

Appendix B

Surface and Flow Field IR Radiation from the Apollo Vehicle Reentering the Earth's Atmosphere

Roy J. Nichols
Thomas W. Tuer
William M. Hamilton
The University of Michigan
Willow Run Laboratories
The Institute of Science and Technology
Ann Arbor, Michigan

January 5, 1966

Source Radiation Characteristics

No direct radiation measurements have been made on a vehicle reentering the earth's atmosphere at super-orbital velocities, except for the recent Project Fire reentry. However, since the results were somewhat inconclusive insofar as defining the spectral distribution of the radiation, a program was initiated at BAMIRAC to predict the surface, gaseous, and particulate radiation.

Surface Radiation

The radiation emitted by a Lambertian surface is a function of its skin temperature and spectral emissivity. Calculated surface temperatures for five limiting Apollo body points as a function of altitude and spectral emissivity measurements* were provided by NASA Manned Spacecraft Center. However, because of the severe thermal gradient over the surface of the vehicle, a more detailed temperature profile was desired. The surface temperatures at 560 body points were determined using a logarithmic interpolation between the five body points on the basis of heat flux to the surface. This procedure is substantiated by the following arguments.

From experimental plasma jet studies, the surface of the heat shield material has been shown to respond instantaneously for high heat inputs (Figure B1):

$$\ln T_w \sim \ln(q/B) \quad .$$

At lower heat inputs, the surface is expected to be in radiative equilibrium; i.e.,

$$q \sim \epsilon\sigma T_w^4$$

or

$$\ln T_w \sim \frac{1}{4} \ln (q/\epsilon\sigma) \quad .$$

Thus, for all except exceedingly low heat inputs $d(\ln T_w)/d(\ln q)$ is constant (differing for different ranges of heat inputs) and a logarithmic interpolation is indicated.

The heat rate was calculated including convective and radiative components, using

$$q = (q_r + q_c) \frac{q_T}{c} \quad ,$$

*Personal communication from George Strouhal, Manned Spacecraft Center, Houston, September 17, 1964.

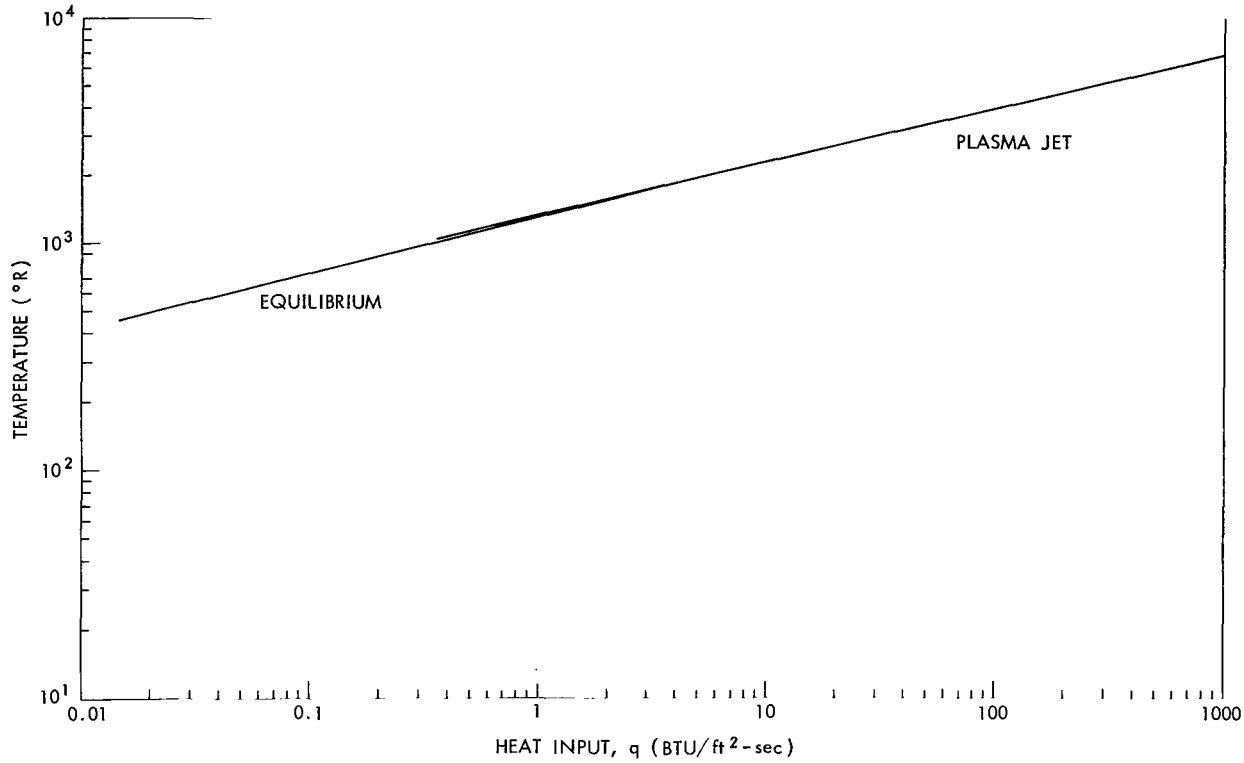

Figure B1—Surface temperature of heat shield as a function of heat input.

where

q_T is the reference heat flux, which is a function of time only,

q_r is the radiative heat flux distribution ratio, independent of time, and

q_c is the convective heat flux distribution ratio, independent of time.

Convective heat distribution over the surface was determined experimentally by NASA. The radiative distribution was assumed proportional to the pressure distribution which was calculated using Newtonian theory. It should be noted that by using the interpolation procedure the surface temperature is independent of the absolute magnitude of the heat flux and simply depends on the relative heat flux profile over the surface.

Having determined the surface temperatures for n body stations, the surface radiation may be calculated. For a given station, the radiant intensity may be written using Planck's function,

$$J_n = \frac{C_1 A_n}{\pi} \int_{\lambda_1}^{\lambda_2} \epsilon(\lambda) \lambda^{-5} \left(e^{(C_2/\lambda T_n)} - 1 \right)^{-1} d\lambda$$

where

T_n is the station temperature,

A_n is the projected area as a function of aspect,

$\epsilon(\lambda)$ is the spectral emissivity,

λ is the wavelength, and

J is the radiant intensity in watts-steradian^{-1}.

Summing over n stations gives the total radiant intensity for the Apollo vehicle.

$$J = \frac{C_1}{\pi} \sum_{1}^{n} A_n \int_{\lambda_1}^{\lambda_2} \epsilon(\lambda) \lambda^{-5} \left(e^{(C_2/\lambda T_n)} - 1 \right)^{-1} d\lambda .$$

Calculations were performed for the undershoot and overshoot Apollo design trajectories at front aspect for wavelength intervals of: 1.8 to 2.7μ, 3.3 to 5.0μ, and 8.0 to 12.0μ (Figures B2 and B3). These show further advantages of the 3.3 to 5.0μ bandpass for our purposes. First, the high

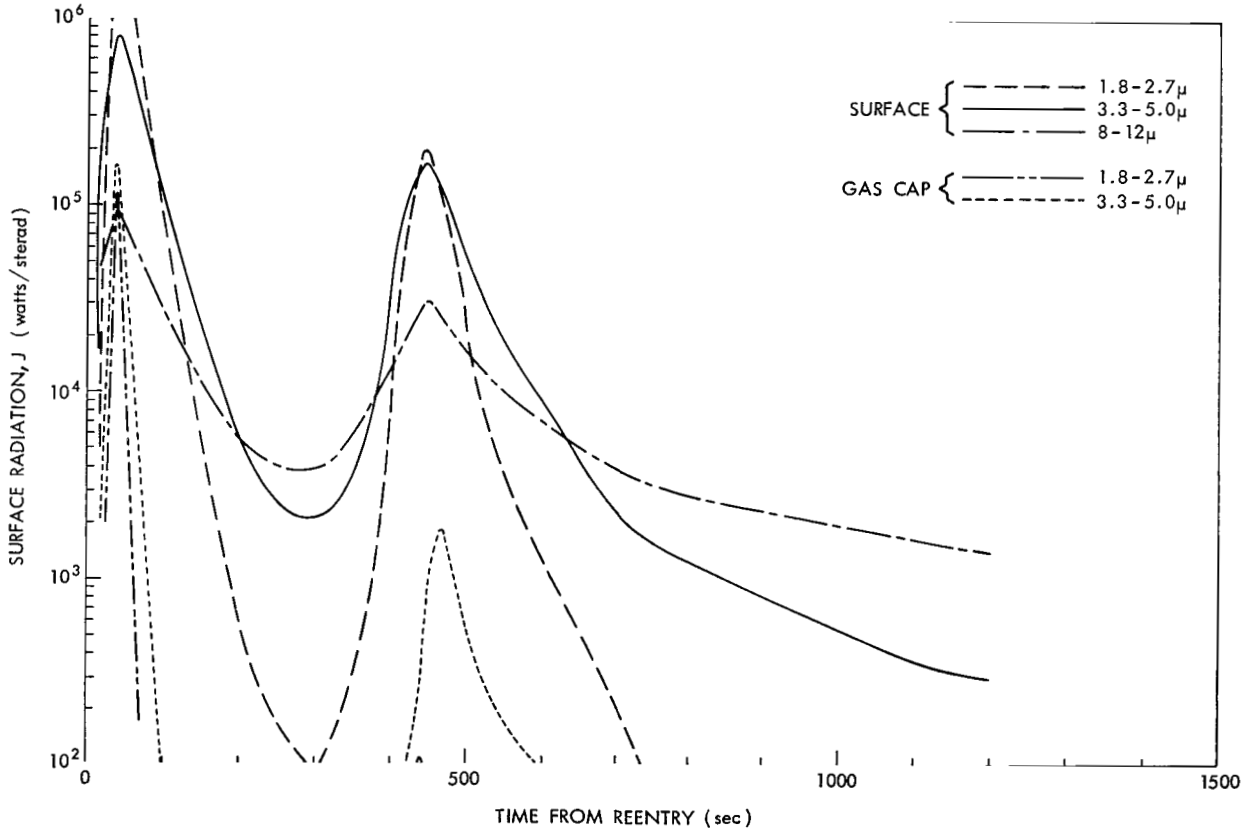

Figure B2—Surface and gas gap radiation from front aspect for an Apollo undershoot trajectory.

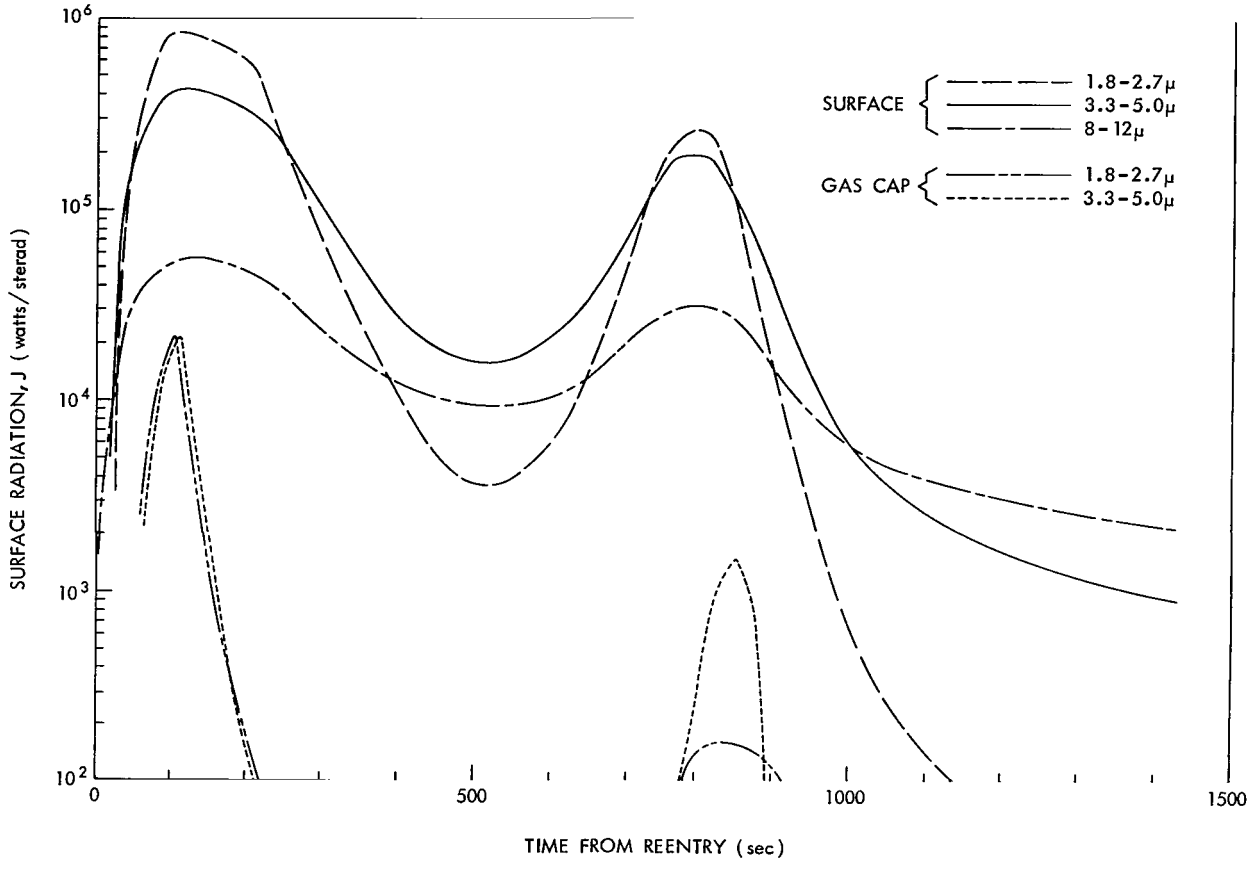

Figure B3—Surface and gas cap radiation from front aspect for an Apollo overshoot trajectory.

initial radiation level will aid in early acquisition, and, second, the moderate dip during the skip portion and the gentle decline following the second radiation peak decreases the likelihood of loss of track prior to an accurate estimation of the impact point.

To show the aspect dependence, families of curves are presented (Figures B4-B15) giving the radiation at selected times for each trajectory-wavelength combination. These curves give the radiation from front to rear aspect in several planes through the vehicle axis (using the angle this plane makes with the pitch plane as a parameter). They exhibit the relatively insensitive behavior of the radiation in the 3.3 to 5.0μ band to aspect even at the highest heating portions of the trajectory, dropping about an order of magnitude from front to rear aspect. As expected, the 8.0 to 12.0μ band is even less sensitive, while the 1.8 to 2.7μ band is highly sensitive, dropping almost two orders of magnitude from front to rear.

Gaseous Radiation

A complete study of the gaseous radiation from the Apollo vehicle should consider contributions from the stagnation region, boundary layer, and near and far wake for all species of pure

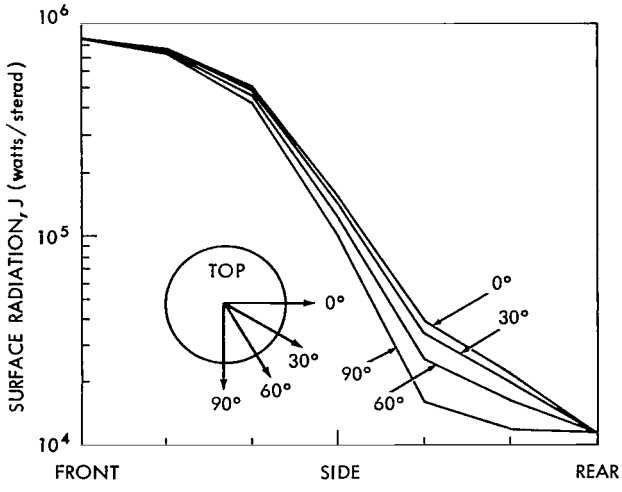

Figure B4—Surface radiation aspect dependence for Apollo overshoot trajectory, 1.8-2.7μ, t = 100 seconds.

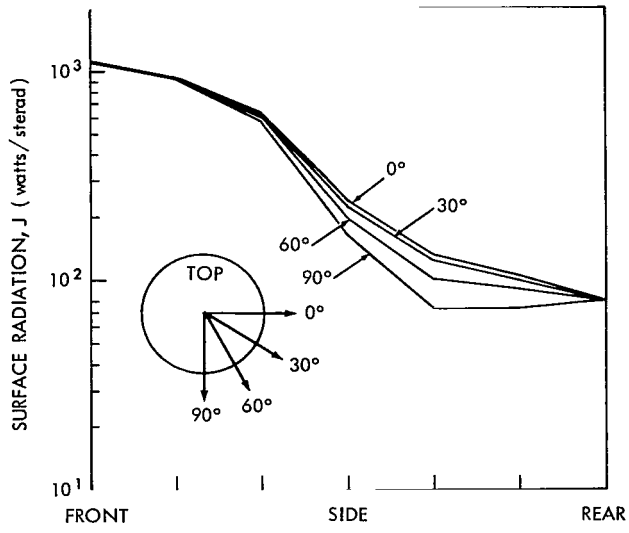

Figure B5—Surface radiation aspect dependence for Apollo overshoot trajectory, 1.8-2.7μ, t = 100 seconds.

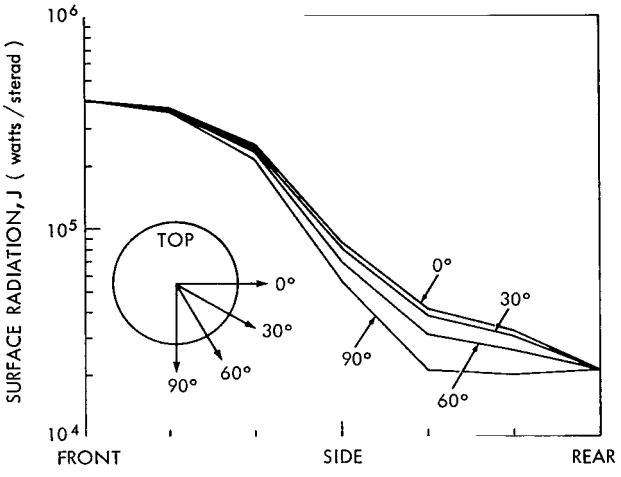

Figure B6—Surface radiation aspect dependence for Apollo overshoot trajectory, 3.3-5.0μ, t = 10 seconds.

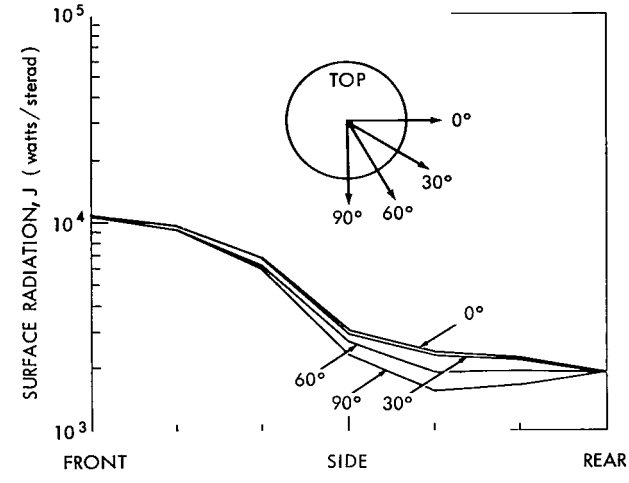

Figure B7—Surface radiation aspect dependence for Apollo overshoot trajectory, 3.3-5.0μ, t = 95 seconds.

and contaminated air, a task far beyond the level of this work. However, by consideration of the flow field chemistry and by restriction of the spectral region to 2-5μ, the list of possible dominant sources is considerably reduced.

The dominant radiation in the near infrared from pure air is produced by NO (important between 1000 - 5000°K), free-free and free-bound interactions of oxygen and nitrogen atoms and molecules with electrons (important between 5000 - 10,000°K), and similar interactions of oxygen and nitrogen ions with electrons (important above 8000°K). Most of this radiation will come from the stagnation region and boundary layer, the hottest portions of the flow field, although it is

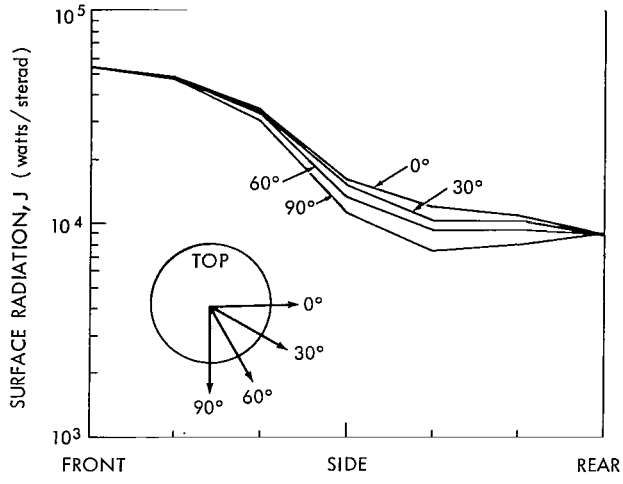

Figure B8—Surface radiation aspect dependence for Apollo overshoot trajectory, 8-12μ, t = 100 seconds.

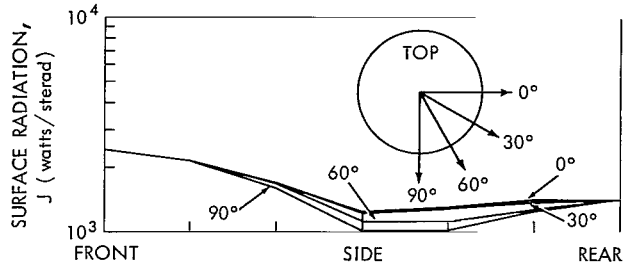

Figure B9—Surface radiation aspect dependence for Apollo overshoot trajectory, 8-12μ, t = 1430 seconds.

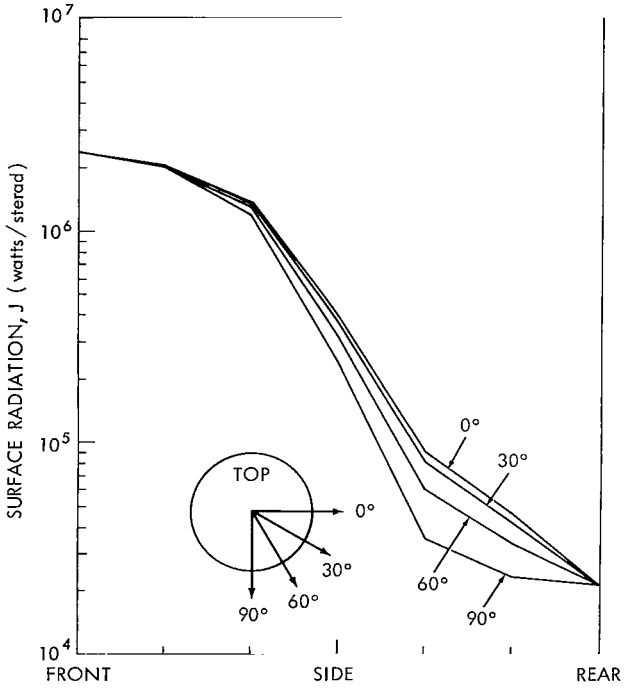

Figure B10—Surface radiation aspect dependence for Apollo undershoot trajectory, 1.8-2.7μ, t = 40 seconds.

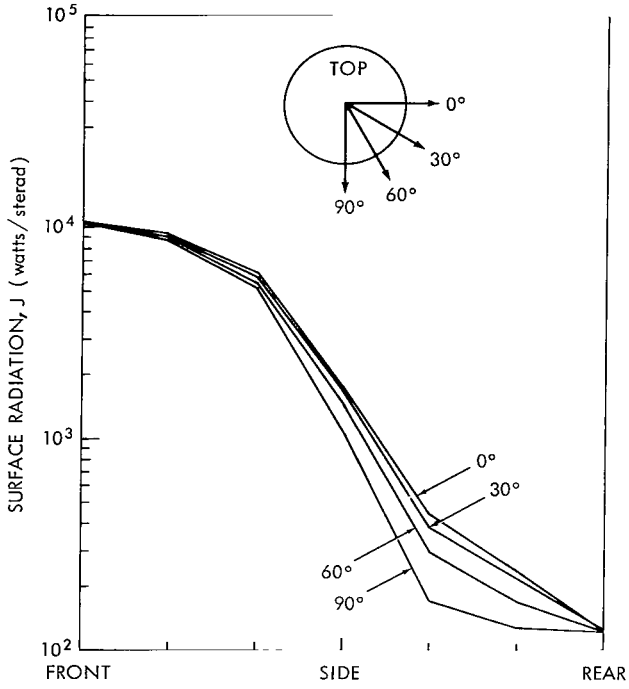

Figure B11—Surface radiation aspect dependence for Apollo undershoot trajectory, 1.8-2.7μ, t = 510 seconds.

possible that contributions from NO in the wake can be important. This latter radiation is nearly impossible to calculate because of the uncertainty in the NO wake chemistry.

Camac and Ryan (Reference B1) suggest the level of total NO wake radiation will be about equal to 10^2 watt-ster^{-1} for a body of one foot nose radius travelling at 22 kft-sec^{-1} at 200 kft. Assuming the radiation scales as $C_D A$, a level of about 10^4 watt-ster^{-1} is suggested for Apollo. This level is about one order of magnitude less than that for the surface radiation, calculated at a

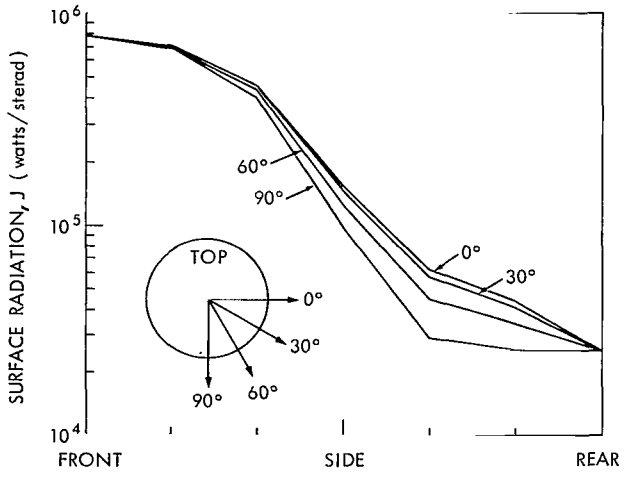

Figure B12—Surface radiation aspect dependence for Apollo undershoot trajectory, 3.3-5.0μ, t = 40 seconds.

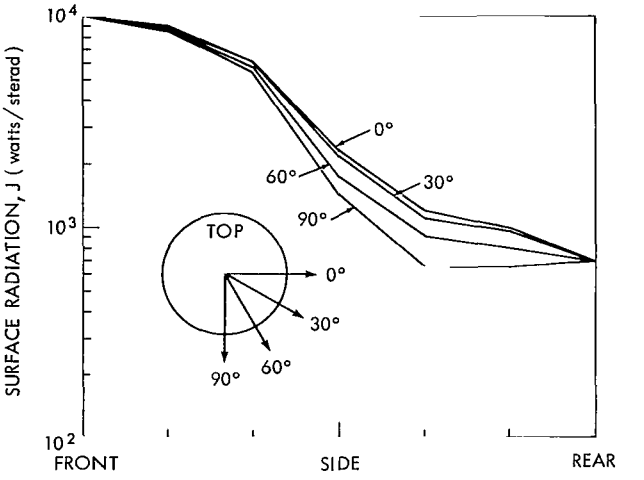

Figure B13—Surface radiation aspect dependence for Apollo undershoot trajectory, 3.3-5.0μ, t = 580 seconds.

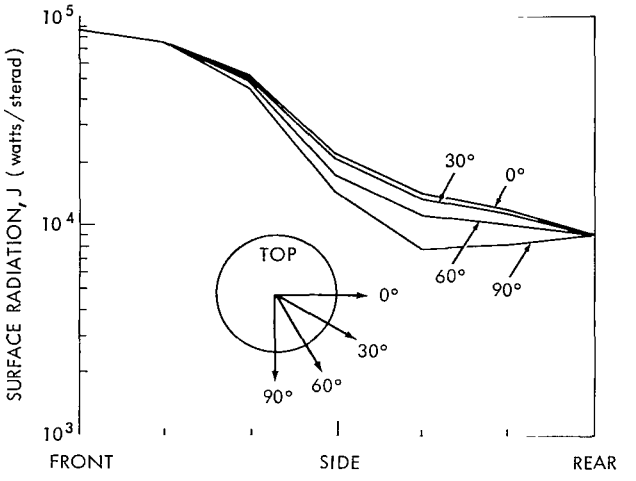

Figure B14—Surface radiation aspect dependence for Apollo undershoot trajectory, 8-12μ, t = 40 seconds.

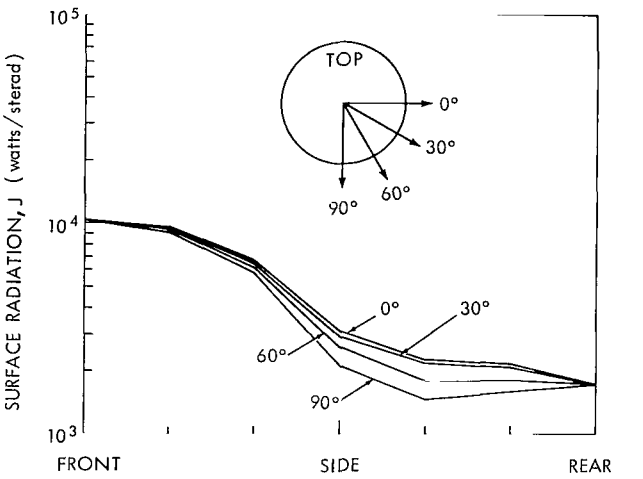

Figure B15—Surface radiation aspect dependence for Apollo undershoot trajectory, 8-12μ, t = 390 seconds.

similar point in the trajectory. In view of the sufficiently intense level of surface radiation calculated at all altitudes, one can only assume that NO wake radiation is *not* a dominant source at any altitude for Apollo.

CO and CO_2 should be the only important molecular ablation products radiating in the 2-5μ region, but because of the long slant paths encountered in any field operation involving Apollo (probably greater than 100 miles) atmospheric absorption should preclude its use.

It thus appears that the major source of gaseous radiation should be from the pure hot air in the stagnation region and boundary layer for altitudes between 300 and 125 kft. The upper limit is set by the atmospheric density; the lower, by the velocity slowdown.

Above about 200 kft, a considerable fraction of the stagnation region and boundary layer (because of the extremely blunt shape, these two regions will be referred to collectively as the gas cap) is not in equilibrium; this must be taken into consideration when the contributions from the various radiating species are summed up. Unfortunately, little study has been made of non-equilibrium radiation in the near infrared. In the ultraviolet and visible, it is well known that non-equilibrium "overshoots" or increased amounts of radiation occur, because the electronic energy levels are not occupied according to a Boltzmann distribution. The little evidence available suggests that significant overshoots do not occur in the infrared, a not unexpected result, since at velocities greater than 20 kft-sec^{-1} one is chiefly concerned with continuum (Kramers) radiation from the interaction of electrons with atoms, molecules, and ions. Hence, only equilibrium radiation has been considered here. Since the preliminary results showed the air radiation to be less than the surface radiation, the omission of non-equilibrium effects should not affect the total amount of signal.

Since the effort could not be expended to set up a computer program to calculate the flow properties in a given number of stream tubes over the body and to sum up the air radiation from each, an approximation was made. For a 25° angle of attack, the pressure distribution derived from NASA data suggested that the temperatures and pressures in the gas cap did not usually change by more than a factor of two as one moved from the stagnation region (located at the top and center of the vehicle face) to the cooler regions (along the outer rim near the bottom). It was therefore decided to divide the gas cap into four regions and to sum up the radiation from each. The gas cap was quartered by defining one boundary as the locus of midpoints between the shock and body and the other as the yaw plane through the body axis so that the gas cap consisted of top-shock, top-body, bottom-body, and bottom-shock sections. The properties in the two top sections were so similar that the gas cap was in effect divided into three regions labelled "A" (top), "B" (bottom-body), and "C" (bottom-front). The properties of region "A" were considered to be those of the stagnation region gas after isentropic expansion to $P_A = 0.8\, P_{stag}$, and those in region "B", to $P_B = 0.4\, P_{stag}$, these pressures being the average values for each section. The properties in region "C" were those immediately behind a normal shock assuming $U = 0.65\, U_\infty$, the average velocity component obtained from NASA shock shapes observed on Apollo models at angle of attack (Reference B2).

Temperatures and densities in the three zones for selected times along the undershoot and overshoot trajectories were calculated. Suffice it here to give them for one trajectory point. For an altitude of 200 kft and a velocity of 19 kft-sec^{-1}, $T_A = 5500°K$, $T_B = 5100°K$, and $T_C = 3400°K$. The respective densities are 3.0×10^{-3}, 1.2×10^{-3}, and 3.0×10^{-3} that of atmospheric (ρ_0). One would then expect the largest amount of radiation to come from region "A" and the least from "C". There are exceptions, however, because NO radiation is not monotonic with temperature, but peaks at about 4000°K.

Once the temperatures and densities were calculated for selected trajectory points, a table relating these properties to the near infrared radiation was required. The tables of General Electric (Reference B3) were basically used, after interpolation and graphic plotting for convenience.

These tables did not account for Kramer's ion radiation, so the graphs for high temperatures were modified by fairing in some later data by Avco (References B4 and B5).

By multiplying the radiation in each region by the volume of that region (obtained from the NASA shock shapes and stand-off distances calculated from simple aerodynamic theory) the radiant intensity in watt-ster^{-1}-μ^{-1} was obtained. Plots of the total radiant intensities in the 2.0-2.6μ and 3.3-5.0μ regions as a function of time for both the overshoot and undershoot trajectories are included in Figures 1 and 2. In general, the air radiation is at least an order of magnitude less than the surface radiation. Because of this result, the calculation of the dependence of the gaseous radiation on aspect angle was felt unnecessary.

Particulate Radiation

Large amounts of carbon char will most certainly be shed into the wake of the Apollo during reentry, especially during the high heating portions of the trajectory. To determine the additional radiation contribution resulting from this char as well as from NO mentioned in the previous section, experimental studies by BAMIRAC at NASA-Ames ballistic range are planned. Hopefully, they will also lend credance to the theoretical predictions of surface and gaseous radiation. The range uses a pellet size of 1-1/2" diameter with counter flow capabilities producing relative velocities up to 35,000 feet per second. It is presently instrumented with eight shadowgraphs, four or five S-1 phototubes (0.5-1.1μ), and twelve photomultipliers (0.5-1.1μ); two or three InSb cells will be added by the University of Michigan to extend the measurements to 5μ.

References

B1. Camac, M., and Ryan, R. J., "Wake Infrared Radiation," Research Note 301 (SECRET), Everett, Mass.: Avco-Everett Research Laboratory, May 1962.

B2. Marvin, J. G., and Kussoy, M., "Apollo Forebody Pressure and Heat-Transfer Distributions in Helium at M_∞ = 20," NASA TM X-854, November 1963 (CONFIDENTIAL).

B3. Breene, R. G., Jr., and Nardone, M., "Radiant Emission from High Temperature Equilibrium Air," Report No. R61SD020, Philadelphia: Space Sciences Laboratory, General Electric Co., May 1961.

B4. Allen, R. A., Taylor, R. L., and Textous, A., "Kramers and Line Radiation from Nitrogen and Air Shocks," Everett, Mass.: Avco-Everett Research Laboratory, May 1963.

B5. Prescott, R., "Image Intensifier Instruments for Acquisition of Weak Targets," Research Note 547, Everett, Mass.: Avco-Everett Research Laboratory, August 1965.

"The aeronautical and space activities of the United States shall be conducted so as to contribute . . . to the expansion of human knowledge of phenomena in the atmosphere and space. The Administration shall provide for the widest practicable and appropriate dissemination of information concerning its activities and the results thereof."

—NATIONAL AERONAUTICS AND SPACE ACT OF 1958

NASA SCIENTIFIC AND TECHNICAL PUBLICATIONS

TECHNICAL REPORTS: Scientific and technical information considered important, complete, and a lasting contribution to existing knowledge.

TECHNICAL NOTES: Information less broad in scope but nevertheless of importance as a contribution to existing knowledge.

TECHNICAL MEMORANDUMS: Information receiving limited distribution because of preliminary data, security classification, or other reasons.

CONTRACTOR REPORTS: Technical information generated in connection with a NASA contract or grant and released under NASA auspices.

TECHNICAL TRANSLATIONS: Information published in a foreign language considered to merit NASA distribution in English.

TECHNICAL REPRINTS: Information derived from NASA activities and initially published in the form of journal articles.

SPECIAL PUBLICATIONS: Information derived from or of value to NASA activities but not necessarily reporting the results of individual NASA-programmed scientific efforts. Publications include conference proceedings, monographs, data compilations, handbooks, sourcebooks, and special bibliographies.

Details on the availability of these publications may be obtained from:

SCIENTIFIC AND TECHNICAL INFORMATION DIVISION

NATIONAL AERONAUTICS AND SPACE ADMINISTRATION

Washington, D.C. 20546